# Optical design and sensitivity optimization of Cryogenic sub-Hz cROss torsion bar detector with quantum NOn-demolition Speed meter (CHRONOS)

Yuki Inoue, <sup>1,2,3,4,\*</sup> Daiki Tanabe, <sup>3,2,4</sup> M.Afif Ismail, <sup>1,2,3</sup> Vivek Kumar, <sup>3,5</sup> Mario Juvenal S Onglao III, <sup>6,2</sup> and Ta-Chun Yu<sup>1,2</sup>

<sup>1</sup>Department of Physics, National Central University, Taoyuan, Taiwan

<sup>2</sup>Center for High Energy and High Field (CHiP), National Central University, Taoyuan, Taiwan

<sup>3</sup>Institute of Physics, Academia Sinica, Taipei, Taiwan

stitute of Particle and Nuclear Studies, High Energy Acceleration Research Organization (KEK), Tsukuba

<sup>4</sup> Institute of Particle and Nuclear Studies, High Energy Acceleration Research Organization (KEK), Tsukuba, Japan <sup>5</sup> Department of Physics, Institute of Applied Sciences and Humanities, GLA University, Mathura 281406, India. <sup>6</sup> National Institute of Physics, University of the Philippines - Diliman, Quezon City 1101, Philippines (Dated: October 30, 2025)

We present the optical design and sensitivity modeling of the 2.5 m Cryogenic sub-Hz cROss torsion-bar detector with quantum NOn-demolition Speed meter (CHRONOS), a triangular Sagnac speed-meter interferometer incorporating power- and signal-recycling techniques. Using ABCD-matrix analysis and Finesse3 simulations, we show that stable eigenmodes are obtained with optimized mirror curvatures and focal placements, achieving mode-matching efficiencies above 99.5 The resulting configuration reaches a quantum-noise-limited strain sensitivity of  $h \simeq 3 \times 10^{-18}$ ,  $\text{Hz}^{-1/2}$  at 1 Hz, with a ring-cavity finesse  $\mathcal{F} \simeq 3.1 \times 10^4$  and round-trip Gouy phase  $\psi_{\text{rt}} \approx 153^\circ$ . The power-recycling cavity detuning ( $\phi_p = -85^\circ$ ) dominates the low-frequency quantum noise, while the signal-recycling cavity detuning ( $\phi_s = 0^\circ$ ) mainly introduces a uniform quadrature rotation. The optimal homodyne angle ( $\zeta_{\text{opt}} \simeq 46^\circ$ ) balances shot-noise and radiation-pressure effects to give the best sensitivity near 1 Hz. Assuming end-mirror reflectivity  $R_{\text{ETM}} = 99.9999\%$  under cryogenic operation at 10 K, CHRONOS can achieve quantum-noise-limited performance on a laboratory scale and serve as a testbed for future long-baseline, cryogenic interferometers probing sub-hertz gravitational waves.

#### I. INTRODUCTION

Gravitational-wave astronomy has advanced rapidly through the success of ground-based interferometers such as LIGO, Virgo, and KAGRA [1–3], and is being further extended into the millihertz band with the upcoming space-based Laser Interferometer Space Antenna (LISA) [4]. However, a sensitivity gap remains in the sub-hertz band. Ground-based detectors are limited at low frequencies by seismic and environmental noise, while space missions cannot adequately cover this band due to constraints on arm length. Several terrestrial efforts specifically target this regime, such as the torsion-bar antenna (TOBA) [5] and Torsion Pendulum Dual Oscillator (TorPeDO) [6], both of which have demonstrated proof-of-principle operation of sub-hertz detectors.

Opening the sub-hertz band would unlock new opportunities for gravitational-wave astronomy. In particular, the merger signals of intermediate-mass black hole (IMBH) binaries exhibit characteristic frequency evolution in this regime. For the Cryogenic sub-Hz cROss torsion bar detector with quantum NOn-demolition Speed meter (CHRONOS) sensitivity scale [7], a facility with an arm length of about 300 m could detect mergers with total mass  $M \sim 10^3 M_{\odot}$  out to 380 Mpc, enabling multi-band observations that bridge LISA and future ground-based detectors. Such observations would provide direct evidence for IMBHs and valuable insights into the formation pathways of supermassive black holes [8]. Moreover, recent O4 observations have begun to reveal the black-hole mass distribution, with several candidate IMBH events already reported [2, 9]. Measurements in the high-mass regime are particularly important for understanding black-hole formation scenarios, and CHRONOS will offer unique access to this parameter space.

In addition, CHRONOS provides unique sensitivity to the stochastic gravitational-wave background ( $\Omega_{\rm GW}$ ) of cosmological origin. With five years of integrated observation, the detector is expected to reach a level of  $\Omega_{\rm GW} \sim 3 \times 10^{-9}$  at 0.2 Hz. This would directly probe early-universe phenomena such as first-order phase transitions and cosmic strings, thus offering rare opportunities to test physics beyond the standard cosmological model [10, 11].

The broader scientific prospects and overall detector concept are discussed in detail in the companion CHRONOS design paper. In this study, we report on the first stage of development: the optical design and sensitivity evaluation of a 2.5 m-scale interferometer. The CHRONOS adopts a triangular Sagnac configuration with output recycling to

<sup>\*</sup> Corresponding author: iyuki@ncu.edu.tw

enhance sensitivity. We investigate suitable sideband signals for controlling multiple cavities, and present design parameters for realistic optical configurations such as dual-recycling cavities. To achieve stable locking of the Sagnac cavity, we compute the mirror-curvature conditions required to reach the desired mode-matching efficiency (99.5%), and confirm consistency across the full optical design. Finally, we calculate sensitivity curves based on the concrete optical layout and discuss the fundamental sensitivity limits of the 2.5 m test facility.

#### II. PRINCIPLE

The readout in this study follows the TOBA framework [5], which is based on the torsional degree of freedom around the z axis. The angular displacement  $\theta$  of a bar-shaped test mass with moment of inertia I, torsional spring constant  $\kappa$ , and loss coefficient  $\gamma$  obeys

$$I\ddot{\theta}(t) + \gamma\dot{\theta}(t) + \kappa\theta(t) = N_{\rm gw}(t),$$
 (1)

where the torque from the gravitational-wave tidal acceleration  $a_i = \frac{1}{2}\ddot{h}_{ij} x^j$  is given by [12, 13]

$$N_{\rm gw}(t) = \frac{1}{2} \ddot{h}_{ij}(t) \,\epsilon_{zki} \,Q_{kj},\tag{2}$$

with

$$Q_{ij} \equiv \int_{V} \rho \left( x_i x_j - \frac{1}{3} r^2 \delta_{ij} \right) dV. \tag{3}$$

In the frequency domain, this becomes

$$\theta(\Omega) = \chi_{\theta}(\Omega) \left[ -\frac{I_{\text{eff}}}{2} \Omega^{2} \left( h_{+} F_{+} + h_{\times} F_{\times} \right) \right],$$

$$\chi_{\theta}(\Omega) \equiv \frac{1}{\kappa - I \Omega^{2} + i \gamma \Omega},$$
(4)

where the torsional resonance  $\Omega_t = \sqrt{\kappa/I}$  is taken to be well below the observational band (sub-mHz to mHz). In the regime  $\Omega \gg \Omega_t$ , the susceptibility reduces to  $\chi_\theta \simeq (-I\Omega^2)^{-1}$ , yielding

$$\theta(\Omega) \simeq \frac{I_{\text{eff}}}{2I} (h_+ F_+ + h_\times F_\times).$$
 (5)

The total and effective moments of inertia are

$$I = \int \rho(x^2 + y^2) \, dV, \qquad I_{\text{eff}} = \int \rho(x^2 - y^2) \, dV, \tag{6}$$

such that  $\eta \equiv I_{\text{eff}}/I \simeq 1$  for an ideal thin rod. In the long-wavelength limit with z-axis incidence, the antenna patterns are [13]

$$F_{+} = \sin 2\alpha, \qquad F_{\times} = -\cos 2\alpha. \tag{7}$$

By combining two orthogonal bars (X and Y) into a differential readout  $\theta = \theta_X - \theta_Y$ , common-mode noise sources such as translational motion and laser intensity fluctuations are suppressed, while retaining sensitivity to linear combinations of the two polarizations [5].

#### III. OPTICAL LAYOUT

An overview of the optical layout is shown in Fig. 2. The experimental apparatus is based on a cross-torsion-bar configuration, with identical optical systems placed in the X and Y arms. After pre-stabilization, the input laser beam first passes through a pre-stabilized laser (PSL) system and an input mode cleaner (IMC), which stabilize and shape the spatial and frequency profiles [14, 15]. The beam is then split at the input beam splitter (IBS) and directed into the Sagnac interferometers of the X and Y arms. Within each arm, the light propagates through a triangular Sagnac ring cavity, and the returning beams are recombined at the output beam splitter (OBS). The phase difference

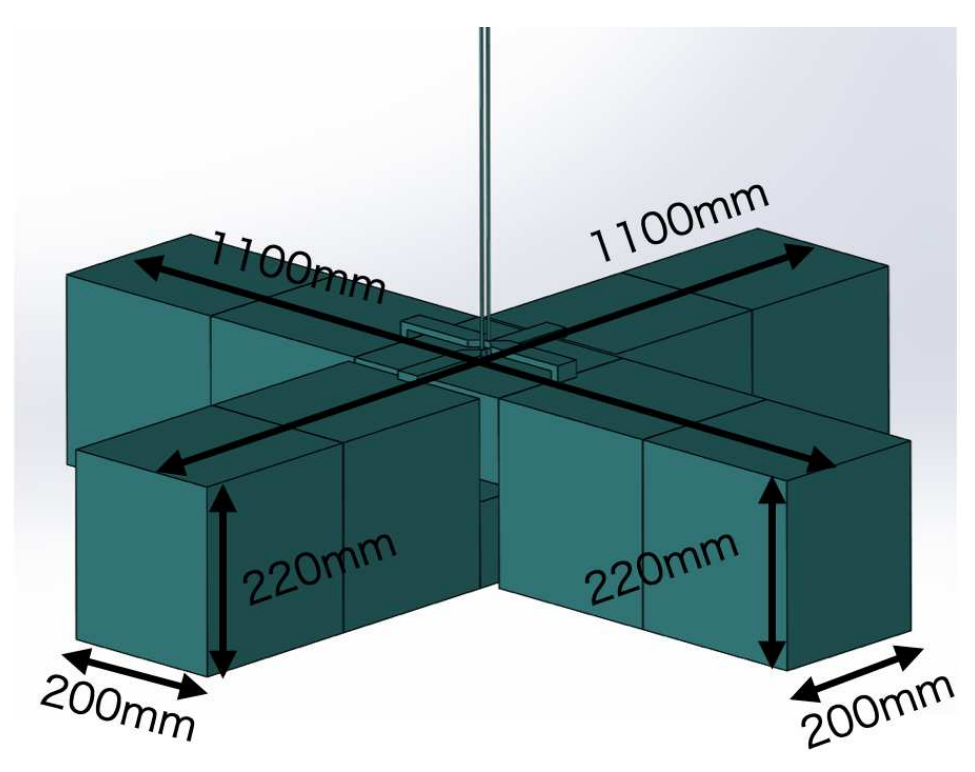


Figure 1: Schematic of the bar-shaped test masses. Each bar has dimensions of 1100 mm in length, 200 mm in width, and 220 mm in height. Two orthogonal bars (X and Y) are suspended at the center to realize differential torsional readout.

between the two arms is extracted as the interferometric signal. For convenience, the following description focuses on the Y arm, but it should be noted that the X arm has an identical optical configuration.

In the overall CHRONOS program, facility scales of 2.5 m, 40 m, and 400 m have been considered, and their sensitivities compared. In this paper, however, we focus on the 2.5 m-scale interferometer as the first step and discuss in detail the sensitivity evaluation [7].

The central part of the interferometer is the triangular Sagnac ring cavity formed by the input test mass (ITM), the middle test mass (MTM), and the end test mass (ETM) located at the ends of each arm. In a simplified description, the closed ring path is defined by six mirrors including the ITM. To ensure proper mode matching, the ETMs and curved mirrors (CMs) are given finite radii of curvature, thereby defining an internal beam waist. The laser injection point is placed about 0.5 m away from the geometric center of the optics, and this asymmetric injection fixes the propagation path of the ring cavity. The Sagnac topology measures the velocity rather than the displacement of the test masses, thereby naturally suppressing radiation-pressure noise at low frequencies [16, 17].

Power-recycling mirror (PRM) is realized by a cavity formed with PRM1–PRM4 and the beam splitter (BS). This configuration enhances the circulating power inside the Sagnac ring without requiring excessively high input laser power. In particular, PR2 provides the main degree of freedom for mode matching: with a finite radius of curvature, it adjusts the external beam waist position and matches it to the internal eigenmode.

At the output port, a signal-recycling mirror (SRM) is installed to control the extraction of gravitational-wave signal sidebands. By tuning the detuning of this cavity, the overall sensitivity curve—especially in the sub-hertz regime—can be reshaped [18]. Signal recycling also provides flexibility in optimizing quantum-noise suppression at low frequencies and sensitivity enhancement at high frequencies [17, 19].

An output mode cleaner (OMC) is placed at the detection port to remove higher-order spatial modes and unwanted carrier leakage before the light reaches the photodetectors to be -40 dB [14]. This ensures that the detected field faithfully reflects the gravitational-wave sidebands of the interferometer. The final output is read out using balanced-homodyne detection (BHD). By interfering the interferometer output with a local oscillator on two photodiodes and subtracting the resulting photocurrents, arbitrary quadratures of the signal can be measured. Compared with conventional DC readout, this method improves quantum-noise performance at low frequencies [20, 21].

All mirrors, beam splitters, and mode cleaners are fully specified in Appendix A. Table VI summarizes the coordinates, incidence angles, radii of curvature, and reflectivities, allowing the optical layout shown here to be exactly reproduced. These parameters provide the foundation for the beam-propagation simulations and sensitivity analysis

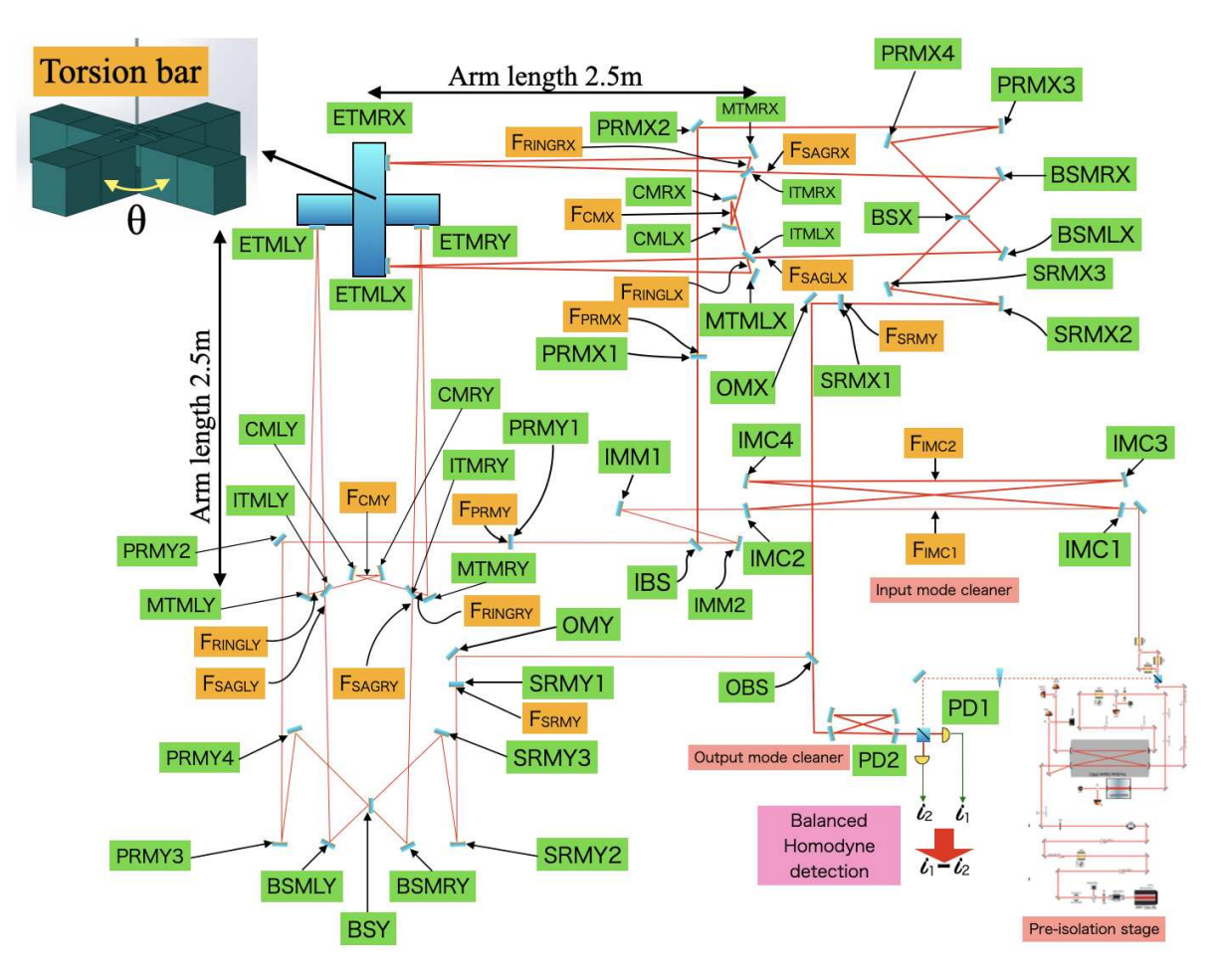


Figure 2: Schematic optical layout of the CHRONOS 2.5 m test facility. After pre-stabilization, the input laser beam passes through the PSL and IMC and is split into the X and Y arms by the IBS. Each arm contains an identical triangular Sagnac ring cavity formed by ITM, MTM, and ETM. For mode matching, the ETMs and CMs are given finite radii of curvature. The laser injection point is offset by about 0.5 m from the geometric center, and this asymmetry determines the closed optical path of the ring cavity. The returning beams are recombined at the OBS and pass through the SRM and OMC before being finally read out by BHD.

presented in later sections.

### IV. CAVITY CONTROL

Before discussing the sensitivity of the 2.5 m interferometer, it is useful to clarify the design philosophy that guided the selection of the topology, cavity lengths, recycling scheme, and control sidebands in this study. The ultimate goal of this work is to construct a laboratory-scale interferometer that is both experimentally feasible and faithfully reflects the requirements of a large-scale CHRONOS detector.

In this work, we adopt a triangular Sagnac topology that measures the *velocity* rather than the *displacement* of the test masses. This feature naturally suppresses radiation-pressure noise in the low-frequency band and is essential for extending the sensitivity toward the sub-hertz regime. The 2.5 m interferometer provides a realistic environment for experimentally validating optical stability, mode matching, control schemes, and quantum-noise readout strategies.

#### A. Sideband frequencies

The starting point of the design is the round-trip length of the ring cavity. If the length of the triangular Sagnac ring is

$$L_{\rm ring} = 5.08 \text{ m},$$

the corresponding free spectral range (FSR) is

$$\mathrm{FSR}_{\mathrm{ring}} = \frac{c}{L_{\mathrm{ring}}} \simeq 59.0 \ \mathrm{MHz}.$$

From this reference, the effective one-way lengths of the power-recycling cavity (PRC) and the signal-recycling cavity (SRC) are determined. The SRC is designed to be half-resonant with respect to itself while remaining resonant with the PRC, such that

$$L_{\rm src} \simeq 5.08 \text{ m}, \qquad \text{FSR}_{\rm src} \simeq 29.5 \text{ MHz},$$

which corresponds to exactly half the ring FSR. Meanwhile, the PRC is set to

$$L_{\rm prc} \simeq 7.62 \text{ m}, \quad \text{FSR}_{\rm prc} \simeq 19.7 \text{ MHz}.$$

These values reproduce the resonant and anti-resonant operating conditions originally established in the LIGO series [22], which define the optimal phase relationships between the power- and signal-recycling cavities to enhance interferometer response at specific frequency bands. While those configurations were first implemented in kilometer-scale detectors, the present design achieves equivalent optical conditions at the 2.5 m scale, demonstrating that the essential interferometric dynamics can be faithfully reproduced within a compact experimental platform.

Based on this configuration, three radio frequency (RF) sidebands are selected. Two of them are used for the main cavity control:

$$f_1 = 29.50 \text{ MHz}, \qquad f_2 = 58.98 \text{ MHz}.$$

The higher frequency  $f_2$  coincides with the ring FSR, being resonant in the PRC and anti-resonant in the SRC. This distinction allows the PRC and SRC degrees of freedom to be separated using a single modulation frequency.

Furthermore, the IMC must filter the carrier light while transmitting both sidebands  $f_1$  and  $f_2$  without loss. To satisfy this requirement, the IMC round-trip length is set to

$$L_{\rm IMC} = 10.17 \text{ m}, \quad \text{FSR}_{\rm IMC} \simeq 14.8 \text{ MHz},$$

and an additional sideband is introduced at

$$f_{\rm IMC} = 44.20 \ \rm MHz.$$

This configuration provides sufficient discrimination for laser frequency stabilization while maintaining consistency with the overall interferometer frequency structure [23, 24].

## B. Control ports and control scheme

The CHRONOS interferometer employs a dual-recycled Sagnac configuration, using multiple detection ports and RF sidebands to stably control the common and differential degrees of freedom of the coupled cavities. This section describes the overall control scheme—including the initial alignment (INI) phase—along with the definition and optical roles of each control port [24, 25].

a. Initial alignment and INI control. The interferometer lock sequence begins with the INI phase, whose purpose is to establish optical alignment and reference signals. In this stage, the positions and orientations of the IMC, PRM, BS, and input steering mirrors are adjusted to stabilize the spatial mode and phase reference of the beam injected into the Sagnac system.

The IMC is a four-mirror bow-tie cavity that serves both as a spatial mode filter and as a frequency reference [23, 25]. Each mirror is suspended by a single-pendulum suspension system, allowing isolation from ground vibrations and precise angular control. The cavity length is maintained by Pound-Drever-Hall (PDH) control [26, 27] using modulation at  $f_{\rm IMC} = 44.235$  MHz. The reflected light is demodulated at the same frequency to produce an error

Table I: Major detection ports and their corresponding control degrees of freedom (DOF) in the CHRONOS dual-recycled Sagnac interferometer. The top row, IMC-INI, represents the initial-alignment and frequency-reference stage in the IMC, where the length of the IMC cavity (IMCL) is maintained by a 44.235 MHz PDH signal. The subsequent ports—REFL, POP, and AS—are used to sense and control the common and differential DOFs of the main dual-recycled Sagnac interferometer (PRCL, CSAG, DSAG, and SRCL). All RF ports use phase-coherent sidebands at  $f_1 = 29.500$  MHz and  $f_2 = 58.980$  MHz, corresponding respectively to the resonance conditions of the PRC and the SRC. The final port, AS-BHD, is a DC readout channel that extracts the velocity component of the DSAG as the speed-meter signal—the scientific output of the interferometer.

Port	RF freq.	Main DOF	Role	Remark
IMC-INI	$44.235~\mathrm{MHz}$	IMCL	IMC length and alignment control	Four-mirror suspended bow-tie cavity
REFL	$29.500~\mathrm{MHz}$	PRCL, CSAG	PRC and common path-length control	Also used for frequency stabilization
POP-A	$58.980~\mathrm{MHz}$	PRCL (aux), CSAG	Common Sagnac mode monitor	Near-field pick-off
POP-B	$58.980~\mathrm{MHz}$	$\overline{\mathrm{DSAG}}$	Differential Sagnac control	Far-field pick-off
AS	$58.980~\mathrm{MHz}$	$\operatorname{SRCL}$	Signal-recycling cavity control	Output port (dark fringe)
AS-BHD	DC	Science (DSAG velocity)	Speed-meter readout	Phase-quadrature homodyne detection

signal, which drives coil-magnet actuators attached to the end mirror to control the length. This configuration follows the KAGRA-style IMC design [25], which employs magnetic actuation of the suspended mirrors rather than piezoelectric (PZT) actuation, enabling large-stroke, low-frequency control with excellent stability. The transmitted beam serves as a monitor for the spatial mode and intensity stability, and its low-frequency component is also used for offset compensation in the laser-frequency control loop [23].

The RF phase reference of the IMC is phase-locked to the modulation sources at  $f_1 = 29.5$  MHz and  $f_2 = 58.980$  MHz, ensuring a common demodulation phase for the Reflection port (REFL) and Pick-off port (POP) detection channels. Once this initial alignment phase is completed, the input beam with matched spatial mode, frequency, and phase is established, allowing transition to the green pre-lock and PRC/SRC control stages.

- b. Reflection port (REFL). The REFL port detects the light reflected from the input mirror of the PRC. This port directly monitors the total reflectivity of the interferometer and provides the primary error signal for the PRC length (PRCL). Demodulation of the reflected light at  $f_1 = 29.5$  MHz produces the PRC error signal via the PDH technique [26, 27]. In addition, the REFL port serves as an auxiliary monitor for the common Sagnac mode (CSAG), corresponding to the average optical path length of the clockwise (CW) and counter-clockwise (CCW) beams, and contributes to maintaining the overall optical resonance and laser-frequency stability.
- c. Pick-off port (POP). The POP port is a pick-off of the intracavity field in the PRC, designed to sense both the common and differential components of the optical field [28]. Two photodiodes are placed at positions with distinct Gouy phases to spatially separate optical modes:
  - POP-A (near field): Located near the PRM, sensitive to the CSAG and the PRCL. This signal is mainly used as an auxiliary channel for common path-length and laser-frequency stabilization.
  - POP-B (far field): Located downstream with a Gouy-phase shift of 45°-90° relative to POP-A, providing high sensitivity to the differential Sagnac mode (DSAG).

Both POP-A and POP-B are demodulated at  $f_2 = 58.980$  MHz. The Gouy-phase difference enables clear separation of the CSAG, PRCL and DSAG in detection.

- d. Antisymmetric port (AS). The AS port corresponds to the output (dark) port of the Sagnac interferometer. When the interferometer is on resonance, the carrier light ideally remains dark at this port (dark fringe). The demodulated signal at  $f_2 = 58.980$  MHz provides the main error signal for the SRC length (SRCL) [24]. Meanwhile, the DC component is read out by BHD, where the velocity signal contained in the DSAG is extracted as the scientific output [20, 21]. The homodyne angle is set near the phase quadrature, and the in-phase component is electronically blended at low frequencies to improve control stability [29].
- e. Comparison with a Fabry-Perot Michelson interferometer. The DSAG corresponds to the DARM degree of freedom in a Michelson interferometer, but in the CHRONOS configuration it represents a velocity-type observable that measures the difference in propagation speed between the CW and CCW beams rather than their positional displacement [16]. Similarly, the CSAG corresponds to the Michelson CARM, representing the common path length coupled to the laser frequency and PRC resonance.

#### V. MODE-MATCHING DESIGN

The eigenmodes of an interferometer are determined using the ABCD-matrix formalism for Gaussian beams [30]. The complex beam parameter q is defined as

$$\frac{1}{q(z)} = \frac{1}{R(z)} - i\frac{\lambda}{\pi w^2(z)},$$
 (8)

where beam radius w(z), the radius of wavefront curvature R(z), and the laser wavelength  $\lambda$  are defined. An optical system is represented by the ABCD matrix

$$M = \begin{pmatrix} A & B \\ C & D \end{pmatrix},\tag{9}$$

and the beam parameter transforms according to

$$q' = \frac{Aq + B}{Cq + D}. (10)$$

For a resonant cavity, the stable eigenmode is obtained by solving q = (Aq + B)/(Cq + D) for the round-trip matrix  $M_{\rm rt}$ . From this, the beam waist  $w_0$ , Rayleigh range  $z_R = \pi w_0^2/\lambda$ , and Gouy phase  $\zeta(z) = \arctan(z/z_R)$  are derived.

The mode matching between two cavities is quantified by the overlap integral of their respective fundamental Gaussian modes:

$$\eta = \left| \frac{\iint E_{\rm in}^*(x, y) E_{\rm cav}(x, y) dx dy}{\sqrt{\iint |E_{\rm in}|^2 dx dy} \sqrt{\iint |E_{\rm cav}|^2 dx dy}} \right|^2, \tag{11}$$

where perfect overlap gives  $\eta = 1$ . Any mismatch in waist size, curvature, or alignment decreases the coupled circulating power and increases the prompt reflection at the input port.

If the beam parameters on the reference plane are  $q_1$  and  $q_2$ , the coupling efficiency can be rewritten as

$$\eta = \left| \frac{2\sqrt{\Re(1/q_1)\Re(1/q_2)}}{1/q_1 + 1/q_2^*} \right|^2. \tag{12}$$

For two coaxial Gaussian beams, the coupling efficiency can be expressed exactly in terms of the waist radii  $w_i$  and wavefront curvature radii  $R_i$  (i = 1, 2) [31]:

$$\eta = \frac{4}{\left(\frac{w_1}{w_2} + \frac{w_2}{w_1}\right)^2 + \left[\frac{\pi w_1 w_2}{\lambda} \left(\frac{1}{R_1} - \frac{1}{R_2}\right)\right]^2}.$$
(13)

This expression provides an intuitive way to evaluate the mode-matching efficiency based on the mismatches of waist size and wavefront curvature, and it is well suited for assessing the design tolerances of high-finesse interferometers such as CHRONOS.

## A. Requirement conditions

In the mode-matching design of the CHRONOS triangular ring cavity, the internal optical loss  $L_{\rm int}$  is sufficiently small—below  $10^{-5}$  (10 ppm)—thanks to high-quality dielectric coatings. Therefore, the dominant factors that determine the optical performance are the external coupling efficiency  $\eta$  and the coupling symmetry between the CW and CCW propagation paths.

The coupling loss is defined as

$$L_{\rm cpl} = 1 - \eta. \tag{14}$$

If the coupling efficiencies for the CW and CCW beams are denoted by  $\eta_{\rm CW}$  and  $\eta_{\rm CCW}$ , respectively, their difference

$$\Delta \eta = \eta_{\rm CW} - \eta_{\rm CCW} \tag{15}$$

represents the coupling asymmetry. The relative asymmetry (i.e., the normalized coupling imbalance) is given by

$$\left| \frac{\Delta \eta}{\eta} \right| = \left| \frac{\eta_{\text{CW}} - \eta_{\text{CCW}}}{(\eta_{\text{CW}} + \eta_{\text{CCW}})/2} \right|. \tag{16}$$

This quantity directly governs the balance of radiation pressure between the CW and CCW beams and determines the stability of the quantum nondemolition (QND) response in the speed-meter interferometer [16].

a. Derivation of the asymmetry condition. The radiation-pressure noise appearing in the output of a speed-meter interferometer can be approximated as [16]

$$S_{x,\mathrm{BA}} \propto \frac{1}{\mathcal{F}^2} + \delta^2,$$
 (17)

where the optical-power asymmetry between CW and CCW beams  $\delta \equiv \Delta \eta/\eta$ , and the cavity finesse  $\mathcal{F}$  are defined respectively. The first term corresponds to the finite-finesse contribution under ideal symmetry, while the second term represents the additional back-action noise caused by coupling asymmetry. To preserve the QND condition (i.e., complete cancellation of radiation pressure), the asymmetry term must be much smaller than the finesse term:

$$\delta^2 \ll \frac{1}{\mathcal{F}^2} \quad \Rightarrow \quad \left| \frac{\Delta \eta}{\eta} \right| \ll \frac{1}{\mathcal{F}}.$$
 (18)

For the CHRONOS cavity,  $\mathcal{F} \simeq 3 \times 10^4$ , thus

$$\frac{1}{\mathcal{F}} \approx 3.3 \times 10^{-5}$$
.

To maintain more than 99% of the radiation-pressure noise cancellation (QND condition), it is reasonable—after including a safety margin—to require

$$\left| \frac{\Delta \eta}{\eta} \right| < 3 \times 10^{-5}. \tag{19}$$

This ensures that the CW/CCW circulating-power imbalance remains below  $10^{-4}$ , allowing stable QND response across the entire detection band.

b. Practical mode-matching efficiency. When the internal loss is sufficiently low, the conventional criterion of keeping the external coupling loss  $(1-\eta)$  more than an order of magnitude smaller than the internal loss is no longer realistic. Considering alignment tolerances, wavefront aberrations, and residual higher-order mode content, the practically achievable upper limit of mode-matching efficiency during design verification is approximately  $\eta \simeq 99.5\%$  [23]. This value is experimentally attainable and ensures both long-term operational stability and reproducibility, while fully satisfying the asymmetry condition  $|\Delta \eta/\eta| < 3 \times 10^{-5}$ .

Therefore, the realistic and sufficient design requirements for the CHRONOS triangular ring cavity are:

$$\eta_{\rm req} \ge 99.5 \%, \qquad \left| \frac{\Delta \eta}{\eta} \right| < 3 \times 10^{-5}.$$

These criteria guarantee that the CW and CCW radiation pressures are precisely balanced, allowing stable high-finesse operation with preserved quantum-nondemolition (QND) sensitivity.

## B. Optimization strategy

The optimization of the radius of curvature is designed to simultaneously satisfy the geometric stability of the cavity eigenmode and the mode-matching efficiency with the external injection beam. In this study, with the mirror positions fixed, the optimal curvature radius  $R_{\rm opt}$  of the curved mirrors (mainly PR2 and the end test masses, ETMs) was numerically determined following the steps below:

- (i) In both the sagittal and tangential planes, the cavity eigenmode parameter  $q_{\text{cav}}$  was obtained using ABCD-matrix analysis [30]. From the resulting mode, the wavefront curvature R(z) and beam radius w(z) were calculated, and the astigmatism (the difference between sagittal and tangential planes) was quantitatively evaluated.
- (ii) A parameter sweep was performed with the incidence angle on the curved mirror as a variable, searching for the condition that minimizes the incidence angle. This suppresses higher-order transverse-mode excitations and minimizes the effect of wavefront aberrations.

Table II: Optimized mode-matching results between the PR/SR cavities and the ring cavities at the ITML and ITMR planes. Listed are the real and imaginary parts of the differential beam parameter ( $\Delta q_{\rm re}$ ,  $\Delta q_{\rm im}$ ), its magnitude  $|\Delta q|$ , differences in wavefront curvature ( $\Delta R$ ), beam radius ( $\Delta w$ ), and the resulting mode-matching efficiency  $\eta$  after optimization. All efficiencies exceed the target threshold of  $\eta \geq 0.995$ . Positive  $\Delta R$  and  $\Delta w$  indicate a larger radius of curvature and beam size in the PR/SR modes relative to the ring mode.

Arm							$\Delta w$ [m]	η [%]
ITML							$-2.65 \times 10^{-5}$	
							$-2.85 \times 10^{-5}$	
	$\mathbf{t}$	PR-Ring	$-2.07 \times 10^{-2}$	$+6.93 \times 10^{-2}$	$7.23 \times 10^{-2}$	+4.31	$+2.35 \times 10^{-5}$	99.7
				$+9.05 \times 10^{-2}$			$+3.29 \times 10^{-5}$	99.5
ITMR	$\mathbf{s}$	PR-Ring	$+7.16 \times 10^{-3}$	$-7.62 \times 10^{-2}$	$7.66 \times 10^{-2}$	+0.80	$-2.94 \times 10^{-5}$	99.6
	$\mathbf{s}$	SR-Ring	$+1.55 \times 10^{-2}$	$-7.92 \times 10^{-2}$	$8.07 \times 10^{-2}$	+0.11	$-3.13 \times 10^{-5}$	99.5
				$+6.21 \times 10^{-2}$			$+2.07 \times 10^{-5}$	
	t	SR-Ring	$-9.08 \times 10^{-3}$	$+8.39 \times 10^{-2}$	$8.44 \times 10^{-2}$	-0.78	$+3.03 \times 10^{-5}$	99.6

- (iii) Geometric symmetry was enforced between the left and right Sagnac rings, imposing a constraint that the CW and CCW eigenmodes must coincide. This guarantees symmetric resonance conditions and beam parameters, ensuring a balanced interferometric response.
- (iv) Within these constraints, the complex beam parameter of the external injection beam,  $q_{\rm in}$ , was fixed, and the mismatch at the output plane was minimized via ABCD propagation:

$$\Delta q = q_{\rm in} - q_{\rm cav}.$$

The optimal curvature  $R_{\rm opt}$  was numerically determined by maximizing the mode-matching efficiency  $\eta$  as the objective function, using the standard Gaussian-beam overlap expressions [31].

(v) For the obtained  $R_{\rm opt}$ , the cavity stability condition  $0 < g_1 g_2 < 1$  was verified, and the round-trip Gouy phase  $\psi_{\rm rt}$  and transverse-mode spacing (TMS) were computed. When these values fall within the stable region and remain nondegenerate, the optimization is considered converged [30].

Through this procedure, the optimal curvature is uniquely determined from both the intrinsic cavity mode and external beam-matching conditions, yielding a stable configuration with minimal optical astigmatism.

#### C. Results

In the first stage of this study, an optimization was performed to maximize the mode-matching efficiency  $\eta$  of the cavity, using the radius of curvature R of each curved mirror as a design variable. The optimization was conducted by determining the cavity eigenmode from ABCD-matrix analysis and by searching for the conditions in which the waist position and wavefront curvature of the injected beam are best matched to those of the cavity mode [30, 31].

The analysis independently evaluated the sagittal (s-plane) and tangential (t-plane) components to account for astigmatism arising from oblique incidence. By adopting the averaged optimal parameters obtained for both planes, the overall modal consistency of the cavity was improved.

As shown in Table VI in Appendix A, the optimal radius of curvature R for each mirror was determined. Under these conditions, at the input test-mass planes (ITML and ITMR), the mode-matching efficiency for the PR-Ring and SR-Ring coupling reached  $\eta \sim 99.6\%$ , well exceeding the practical requirement of  $\eta_{\rm req} \geq 99.5\%$  [23].

The differential beam parameters  $\Delta q$ , wavefront-curvature difference  $\Delta R$ , beam-radius difference  $\Delta w$ , and corresponding efficiencies  $\eta$  obtained at each coupling point are summarized in Table II. In all cases,  $|\Delta q| \lesssim 9 \times 10^{-2}$  m and  $|\Delta w| \lesssim 3 \times 10^{-5}$  m, indicating that the coupling loss remains well below the internal-loss budget.

A few-millimeter difference was observed between the sagittal and tangential focal positions, but this remains within the acceptable range of astigmatism and was confirmed to have negligible impact on  $\eta$ . The focus positions and corresponding beam-waist radii are summarized in Table III.

In conclusion, the obtained set of curvature radii simultaneously maximizes the mode-matching efficiency and satisfies the requirements of geometric symmetry and optical stability. Thus, the CHRONOS PR/SR cavities and ring cavities achieve high-efficiency, stable coupling, providing a solid foundation for subsequent stability analyses and quantum-noise evaluations.

Table III: Beam waist  $w_0$  at each defined focus for sagittal and tangential planes. The positions of the foci are shown in Fig. 2.

Plane	Focus	$\bar{w}_0 \; (\mathrm{mm})$
s	$F_{\text{RINGLY}}, F_{\text{RINGRX}}$	0.452
S	$F_{\mathrm{RINGRY}}, F_{\mathrm{RINGLX}}$	0.455
S	$F_{\text{CMY}}, F_{\text{CMX}}$	0.045
S	$F_{\text{SAGLY}}, F_{\text{SAGRX}}$	0.452
S	$F_{\text{SAGRY}}, F_{\text{SAGLX}}$	0.455
S	$F_{PRMY}, F_{PRMX}$	2.617
S	$F_{\text{SRMY}}, F_{\text{SRMX}}$	2.640
t	$F_{\text{RINGLY}}, F_{\text{RINGRX}}$	0.455
$\mathbf{t}$	$F_{\mathrm{RINGRY}}, F_{\mathrm{RINGLX}}$	0.457
$\mathbf{t}$	$F_{\text{CMY}}, F_{\text{CMX}}$	0.046
$\mathbf{t}$	$F_{\text{SAGLY}}, F_{\text{SAGRX}}$	0.455
$\mathbf{t}$	$F_{\text{SAGRY}}, F_{\text{SAGLX}}$	0.457
$\mathbf{t}$	$F_{PRMY}, F_{PRMX}$	2.604
t	$F_{ m SRMY}, F_{ m SRMX}$	2.630

#### D. Stability evaluation (cavity eigenmode stability analysis)

Using the optimized curvature radii R obtained from the mode-matching optimization, stability analyses were performed for the left and right ring cavities based on both ABCD-matrix calculations and FINESSE3 simulations [30]. In the evaluation, full width at half maximum (FWHM), pole frequency, and the round-trip Gouy phase  $\psi_{\rm rt}$  and transverse mode spacing (TMS) for the sagittal and tangential planes were calculated [30].

The results are summarized in Table IV. In all cavities, the round-trip Gouy phases satisfy  $0^{\circ} < \psi_{\rm rt} < 180^{\circ}$ , corresponding to the stable-cavity condition  $0 < g_1 g_2 < 1$ . In particular, the Gouy phases for the sagittal and tangential planes agree around 153°, confirming the formation of stable eigenmodes in both sagittal and tangential directions.

The obtained finesse,  $\mathcal{F} = 3.14 \times 10^4$ , and free spectral range, FSR = 58.98 MHz, yield a resonance linewidth of 1.88 kHz and a cavity pole frequency (half-width at half maximum) of 939 Hz, demonstrating that the ring cavity possesses sufficiently high optical storage time and stability [23, 26].

Table IV: Simulated stability and optical parameters of the left and right ring cavities after optimization.

Cavity	Plane	$\psi_{\rm rt} \ [{ m deg}]$	TMS [MHz]	FSR [MHz]	Pole [Hz]
Left ring	S	153.3	50.2	59.0	939.1
Left ring	$\mathbf{t}$	153.0	50.1	59.0	939.1
Right ring	$\mathbf{s}$	153.0	50.1	59.0	939.1
Right ring	$\mathbf{t}$	152.7	50.0	59.0	939.1

From these results, both the left and right ring cavities are confirmed to be stable, with the Gouy-phase difference between the s- and t-planes smaller than  $0.6^{\circ}$  and the difference in transverse-mode spacing less than 0.2 MHz. This indicates excellent modal consistency between the two cavities, which contributes to suppressing higher-order mode excitation and ensuring the stable operation of the entire interferometer [30]. Moreover, the obtained finesse and pole-frequency values satisfy the design requirements of the CHRONOS interferometer for high optical storage time and quantum-noise-limited sensitivity [23].

# VI. SENSITIVITY ANALYSIS

The sensitivity of the 2.5 m CHRONOS interferometer is determined by the interplay between quantum noise and technical noise sources. In this study, the optical and mechanical parameters were set to the values listed in Table V, which define the *optimal operating point*. These values are chosen to balance the contributions of shot noise, radiation-pressure noise, and coating thermal noise, optimizing the detector sensitivity around 1 Hz.

In the first part of this section (Sec. VIA), a complete quantum-noise model including the input-output relations and effective optomechanical coupling is introduced. In the latter part, numerical simulations using FINESSE3 are presented to show the resulting sensitivity curves, focusing on the effects of PRC detuning, SRC detuning, and homodyne detection angle. Furthermore, the contribution of the ETM coating thermal noise is quantitatively evaluated, as it

Table V: Assumed optimal optical and mechanical parameters for the 2.5 m CHRONOS interferometer. In the CHRONOS phase convention, the detuning phase of the power-recycling cavity (PRC) is defined with respect to the 0° baseline, whereas both the signal-recycling cavity (SRC) and the homodyne detection phase are referenced to the 90° baseline. This convention is consistently used throughout the detuning and quadrature-rotation analysis.

Definition	Symbol	Value
Signal-recycling mirror reflectivity	$R_s$	0.5
Power-recycling mirror reflectivity	$R_p$	0.9
Input test-mass reflectivity	$R_i$	0.9999
Input laser power	$P_{ m in}$	1 W
Circulating power in arm cavity	$P_{\rm arm}$	444 W
PRC detuning phase	$\phi_p$	$-85^{\circ}$
SRC detuning phase	$\phi_s$	0°
Homodyne detection angle	ζ	$46^{\circ}$
Ring-cavity finesse	$F_{\rm ring}$	$3.14 \times 10^4$
Beam radius on ETM	w	2.6  mm
ETM mass	$M_{ m ETM}$	171 kg
ETM moment of inertia	$I_{ m ETM}$	$19.9 \text{ kg m}^2$
Torsion-bar length	$L_{\rm bar}$	1 m
Geometrical coupling factor	$\eta$	0.936

sets the lower sensitivity limit in the mid-frequency band [32, 33]. A summary of the suspension and thermal noise sources is given in the Appendix B. The intensity noise is calculated in Tanabe et. al. [34].

Through this hierarchical analysis, the impact of optical parameters and material choices on interferometer performance is systematically clarified, providing a guideline for optimization in future CHRONOS designs.

#### A. Noise model

The interferometer's quantum noise is expressed in terms of the measured angular displacement  $\theta$ . Following the Buonanno-Chen formalism [22], we use the two-photon representation [35]. In this method, we define the input and output quadrature vectors as

$$\mathbf{a} \equiv \begin{pmatrix} a_1 \\ a_2 \end{pmatrix}, \qquad \mathbf{b} \equiv \begin{pmatrix} b_1 \\ b_2 \end{pmatrix}.$$
 (20)

where the input quadrature vector of the interferometer a is denoted. The amplitude quadrature (in-phase component)  $a_1$  and the phase quadrature (out-of-phase component)  $a_2$  are represented. The corresponding output quadrature vector b is also defined. With these definitions, the input-output relation can be written as

$$\boldsymbol{b} = \frac{1}{M} \left[ e^{2i(\beta_{\text{sag}} + \Phi_s)} C \boldsymbol{a} + \sqrt{2\mathcal{K}_{\text{sag}}} t_s e^{i(\beta_{\text{sag}} + \Phi_s)} \boldsymbol{D} \frac{\theta}{\theta_{\text{SQL}}} \right], \tag{21}$$

where the transmittance of SRM  $t_s$  and its phase delay  $\Phi_s$  are obtained. The standard quantum limit (SQL) for angular displacement is [36]

$$\theta_{\text{SQL}} = \sqrt{\frac{2\hbar}{I\Omega^2}}.$$
 (22)

The phase accumulated in the arm cavity is

$$\beta = \arctan\left(\frac{\Omega}{\gamma}\right), \qquad \beta_{\text{sag}} = 2\beta + \frac{\pi}{2}.$$

The Sagnac-topology optomechanical coupling becomes

$$\kappa_{\rm sag}(\Omega) = 4 \kappa(\Omega) |H_{\rm PRC}|^2 \sin^2 \beta_{\rm sag},$$
(23)

where the frequency-dependent coupling  $\kappa(\Omega)$  and cavity bandwidth  $\gamma$  follow the definitions in Ref. [37]. The PRC transfer function is

$$H_{\rm PRC} = \frac{\sqrt{T_p}}{1 - \sqrt{R_p} e^{2i\tau_p \Omega} r_{\rm ifo}},$$

and the effective interferometer reflectivity (including Sagnac propagation) is

$$r_{\rm ifo} = i |r_{\rm loop}| \sin(\beta_{\rm sag} + \tau_{\rm sag}\Omega),$$

where the one-way propagation time in the Sagnac loop  $\tau_{\rm sag}$  and effective reflectance in ring cavities and Sagnac loop  $r_{loop}$  are defined.

The overall quantum-noise spectral density is finally expressed as

$$\theta = \frac{\theta_{\text{SQL}}}{\sqrt{2\mathcal{K}_{\text{sag}}(1 - r_s^2)}} \sqrt{\frac{\boldsymbol{\nu}^{\mathsf{T}}G\boldsymbol{\nu}}{\boldsymbol{\nu}^{\mathsf{T}}Q\boldsymbol{\nu}}},\tag{24}$$

where the homodyne detection vector  $\boldsymbol{\nu}^{\mathsf{T}} = (\cos \zeta, \sin \zeta)$  is defined. The G and Q matrices describe the amplitudephase quadrature correlations induced by detuning and optomechanical coupling. Diagonalization yields an effective coupling constant  $\kappa_{\mathrm{eff}}$  and an effective homodyne angle  $\zeta_{\mathrm{eff}}$ , from which the final quantum-limited sensitivity can be evaluated.

## B. Optical Absorption and Mechanical Loss in Coatings

The optical coatings of the end test masses (ETMs) play a decisive role in setting both the quantum- and thermalnoise limits of the interferometer. Two major loss mechanisms—optical absorption and mechanical loss—must be simultaneously minimized to achieve the target sensitivity in the sub-hertz regime.

a. Optical absorption. Even ppm-level absorption leads to increased intracavity loss, reducing the effective reflectivity of the recycling cavities and lowering the circulating optical power [38]. Because both shot noise and radiation-pressure noise scale with optical power, quantum noise is highly sensitive to absorption: an increase in absorption simultaneously raises the shot-noise floor and reduces the radiation-pressure back-action, thereby rebalancing the overall quantum-noise spectrum.

Figure 3 compares shot noise and radiation-pressure noise for different ETM coating reflectivities. The variation in shot noise is small, since it mainly depends on the circulating arm power, whereas radiation-pressure noise increases significantly at low frequencies due to incomplete back-action cancellation when the interferometer reflectivity  $r_{\rm ifo}$  is reduced. This behavior is further illustrated in Fig. 4, which shows the degradation of quantum-nondemolition (QND) suppression under reduced  $r_{\rm ifo}$ .

In CHRONOS, suppression of optical absorption is pursued through the development of advanced low-loss coatings. Plasma-enhanced chemical vapor deposition (PECVD)  $SiN/SiO_2$  and SiON multilayers have demonstrated mechanical-loss angles on the order of  $10^{-5}$  at 100 Hz and room temperature [39, 40]. However, their optical absorption remains higher than required for sub-hertz operation. Low-pressure chemical vapor deposition (LPCVD) coatings are currently being investigated as an alternative, offering the potential to reduce absorption while preserving low mechanical loss. A detailed study of LPCVD absorption properties is presented in V. Kumar *et al.* [41].

b. Mechanical loss. The mechanical-loss angle of the coating layers directly determines the amplitude of Brownian thermal fluctuations [32, 33]. At the 2.5 m CHRONOS scale, this coating Brownian noise defines the mid-frequency sensitivity floor, even under cryogenic operation. Experiments have shown that at  $T \approx 10$  K, typical ion-beam-sputtered (IBS) coatings exhibit loss peaks due to structural relaxation in the amorphous layers [42, 43]. By contrast, annealed SiON coatings demonstrate significantly lower loss at cryogenic temperatures, confirming their potential for next-generation cryogenic interferometers [39, 40].

Figure 5 presents the total quantum-noise spectra, including shot noise, radiation-pressure noise, and other technical noise sources. In the 0.1-10 Hz band, where seismic noise dominates, the coating-related effects still determine the overall sensitivity. To achieve the CHRONOS sensitivity goal, the total effective coating loss angle must satisfy  $\phi_c^{\rm eff} \leq 10^{-5}$  at cryogenic temperatures, while maintaining a reflectivity of  $R \sim 99.9999\%$ . This dual optimization—simultaneous reduction of optical absorption and mechanical loss— is essential to sustaining the high finesse  $(\mathcal{F} \simeq 3.1 \times 10^4)$  and quantum-noise-limited performance required for the CHRONOS sub-hertz interferometer.

# C. Impact of power-recycling cavity detuning

The power-recycling cavity (PRC) plays a central role in enhancing the circulating optical power and shaping the quantum-noise spectrum of the interferometer. Importantly, the PRC reflectivity is not chosen to strictly satisfy resonance for the carrier field; instead, it is deliberately shifted from the exact resonance condition as a result of optimization against low-frequency losses and radiation-pressure noise. This approach follows the same philosophy as

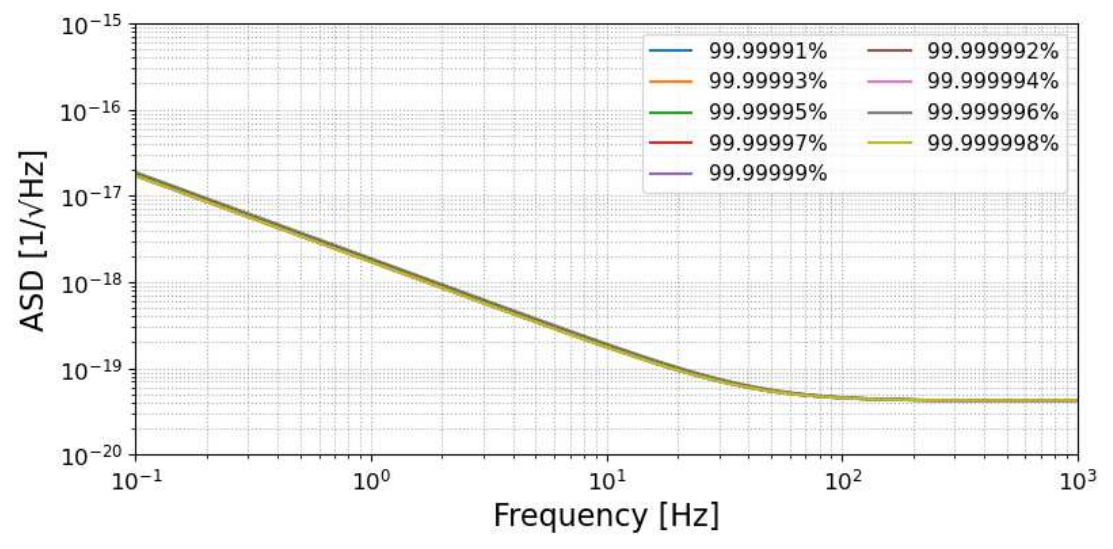


Figure 3: Comparison of shot noise and radiation-pressure noise for varying ETM reflectivity.

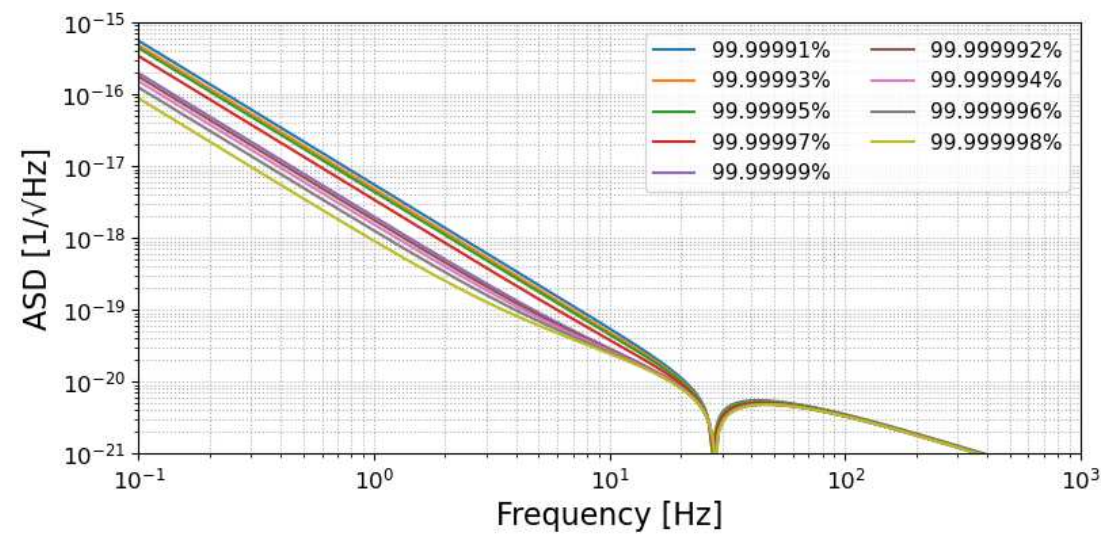


Figure 4: Radiation-pressure noise at low frequencies, illustrating degradation of QND suppression with reduced  $r_{\rm ifo}$ .

detuned signal-recycling interferometers [37], but here it is applied in a unique way to CHRONOS. This adjustment enables the interferometer to suppress sensitivity degradation at low frequencies while maintaining balanced performance across the detection band. Thus, the PRC is not only an element to enhance power, but also a strategic control parameter to optimize the distribution of quantum noise over the full observation band.

When the PRC is detuned by a phase  $\phi_p$ , its transfer function  $H_{\text{PRC}}$  is modified, directly affecting the effective optomechanical coupling coefficient  $\kappa_{\text{sag}}$ . Physically, PRC detuning alters the balance between the amplitude and phase quadratures of the circulating field, shifting the interference conditions between them. As a result, the frequency dependence of shot noise and radiation-pressure noise is reshaped, and the noise ellipse in quadrature space rotates. Therefore, PRC detuning functions as a powerful parameter for controlling the overall noise structure of the interferometer.

Figure 6 shows the impact of PRC detuning on shot noise. Since shot noise is inversely proportional to the circulating arm power, any deviation from the optimal point modifies the stored power and correspondingly changes the shot-noise floor. As illustrated, both positive and negative detuning change the circulating arm power, causing a uniform variation in the shot noise across the high-frequency region. Hence, the behavior of shot noise under PRC detuning can be fully understood as a direct reflection of the change in circulating power relative to the optimal point.

Figure 7 shows the corresponding radiation-pressure noise. In contrast to traditional torsion-bar detectors, radiation-pressure noise in CHRONOS arises not solely from photon-number fluctuations but from a combination of the back-action correlation term and the change in radiation pressure induced by the carrier field. At the optimal point,

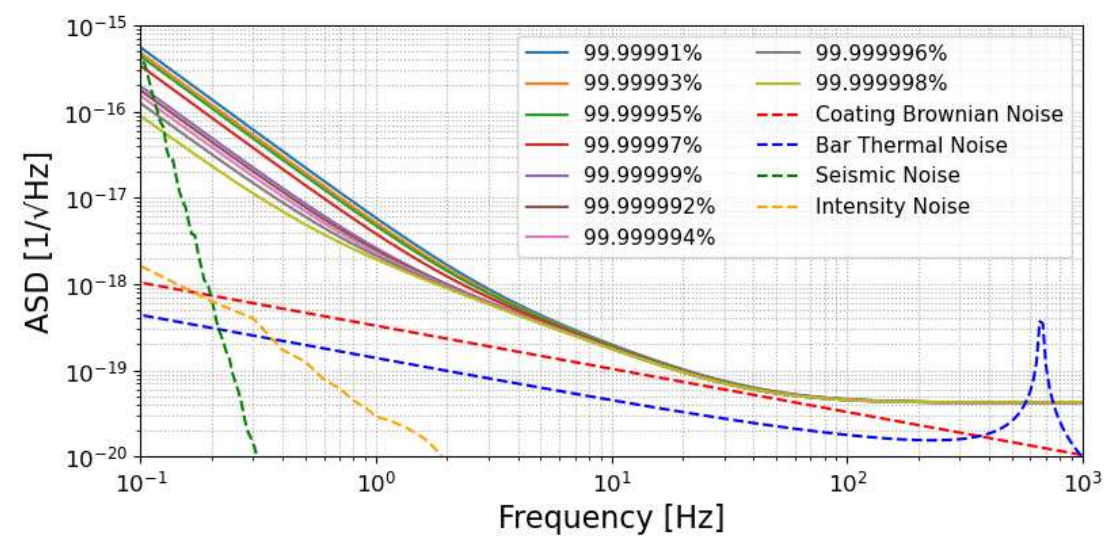


Figure 5: Total quantum-noise spectra including shot noise, radiation-pressure noise, and other technical noise sources. Coating effects dominate the sensitivity in the 0.1-10 Hz band. The intensity noise is calculated elsewhere [34].

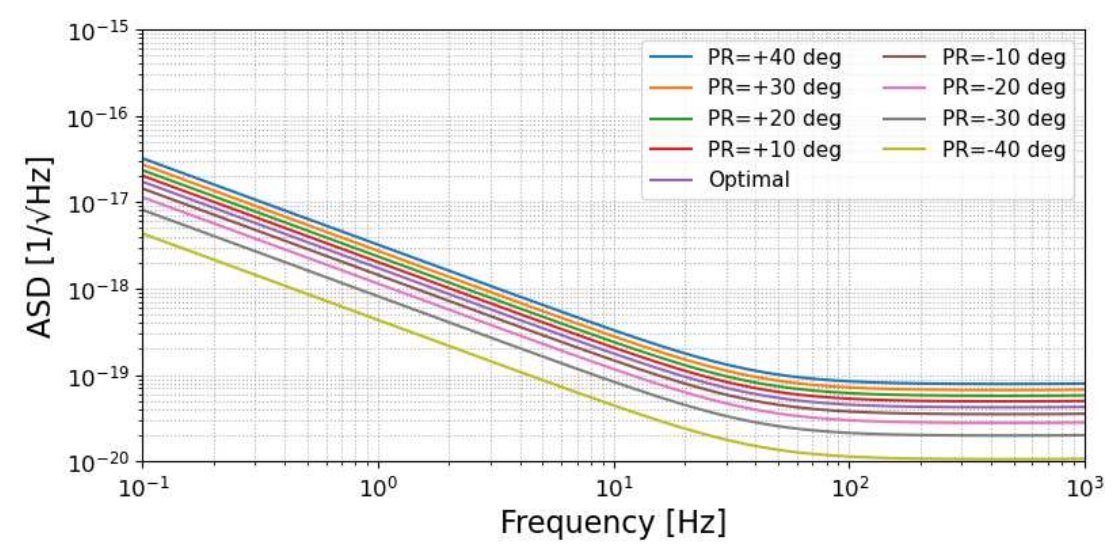


Figure 6: Impact of PRC detuning on shot noise. The variation is explained by the change in circulating arm power relative to the optimal point.

these contributions are balanced with the shot noise, yielding the best sensitivity around 1 Hz. Deviations from this condition break the balance, leading to a rapid increase in low-frequency radiation-pressure noise. Both positive and negative detuning increase the noise, and the effect is significantly more pronounced than for shot noise, emphasizing that PRC detuning dominantly sets the low-frequency sensitivity of CHRONOS.

Finally, Fig. 8 presents the total noise spectra including shot noise, radiation-pressure noise, and other technical noise sources such as seismic and suspension noise. It is evident that at the optimal point these contributions balance each other, providing the best sensitivity near 1 Hz. Away from this point, low-frequency radiation-pressure noise or high-frequency shot noise quickly dominates, leading to degraded sensitivity. This result highlights a unique aspect of CHRONOS: while conventional Michelson interferometers typically employ signal-recycling (SR) detuning to reconfigure their sensitivity curves [37], CHRONOS achieves sensitivity optimization primarily through PR detuning. Thus, PRC detuning represents a distinctive design feature of CHRONOS, enabling a new optimization strategy for suppressing quantum noise in the sub-hertz band.

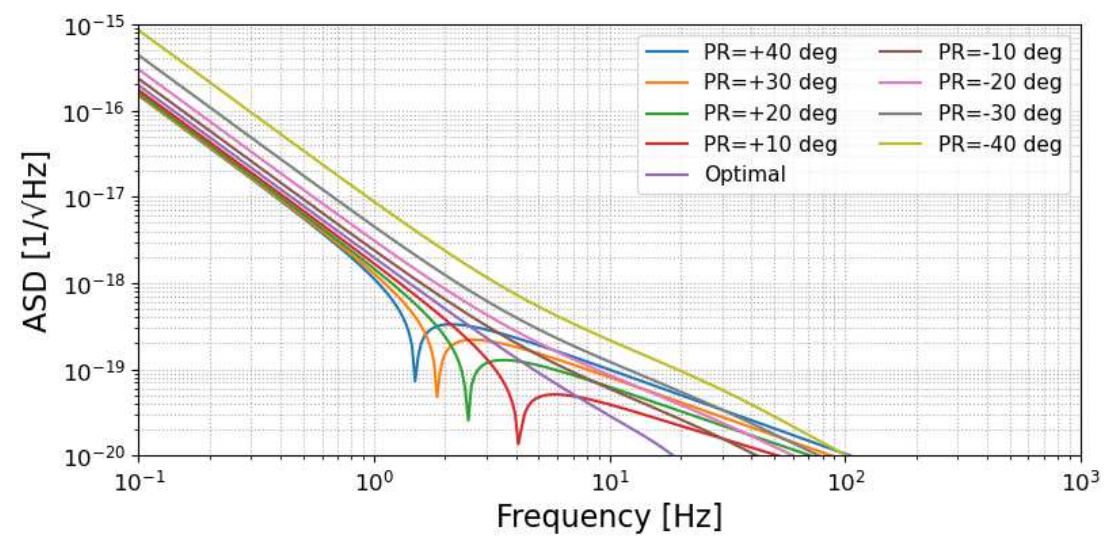


Figure 7: Impact of PRC detuning on radiation-pressure noise. At the optimal point, back-action correlations and carrier-induced radiation pressure balance with shot noise to yield the best sensitivity near 1 Hz.

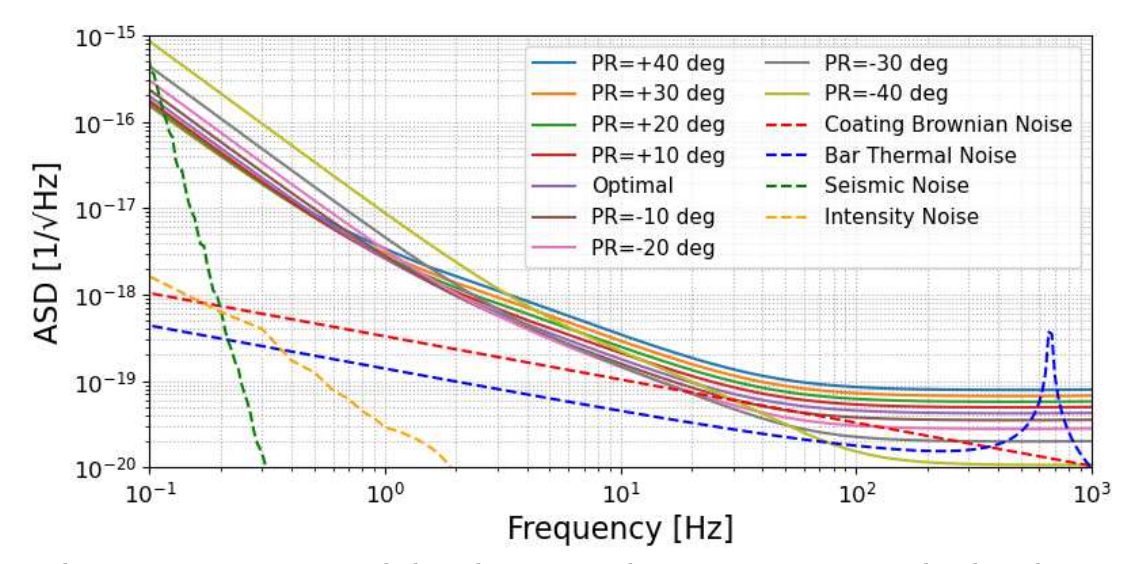


Figure 8: Total quantum-noise spectra including shot noise, radiation-pressure noise, and technical noise sources. The optimal point balances the three contributions, while detuning leads to degraded sensitivity. The intensity noise is calculated in elsewhere [34]

#### D. Impact of signal-recycling cavity detuning

The signal-recycling mirror (SRM) serves as a key optical element that reshapes the interferometer's frequency response by recycling the signal sidebands, thereby improving overall sensitivity. By tuning the reflectivity and detuning phase of the SRM, the signal-recycling cavity (SRC) can redistribute the detector's response between low and high frequencies [37]. However, in the CHRONOS configuration, detuning the SRC away from resonance does not improve the overall sensitivity.

Figure 9 shows the effect of SRC detuning on shot noise. At resonance ( $\phi_s = 0$ ), the signal sidebands are optimally transmitted to the output port, minimizing the shot-noise floor across a broad frequency range. When the SRC is detuned, however, the amplitude ( $a_1$ ) and phase ( $a_2$ ) quadratures in the two-photon formalism become mixed, causing a rotation of the optical field basis in quadrature space. This mixing corresponds to a  $90^{\circ}$  quadrature rotation around the optical phase space, which modifies the detected combination of amplitude and phase components. As a result, the shot noise changes uniformly across the frequency band, effectively shifting the entire sensitivity curve upward or downward depending on the detuning phase. Thus, SRC detuning does not enhance sensitivity in any

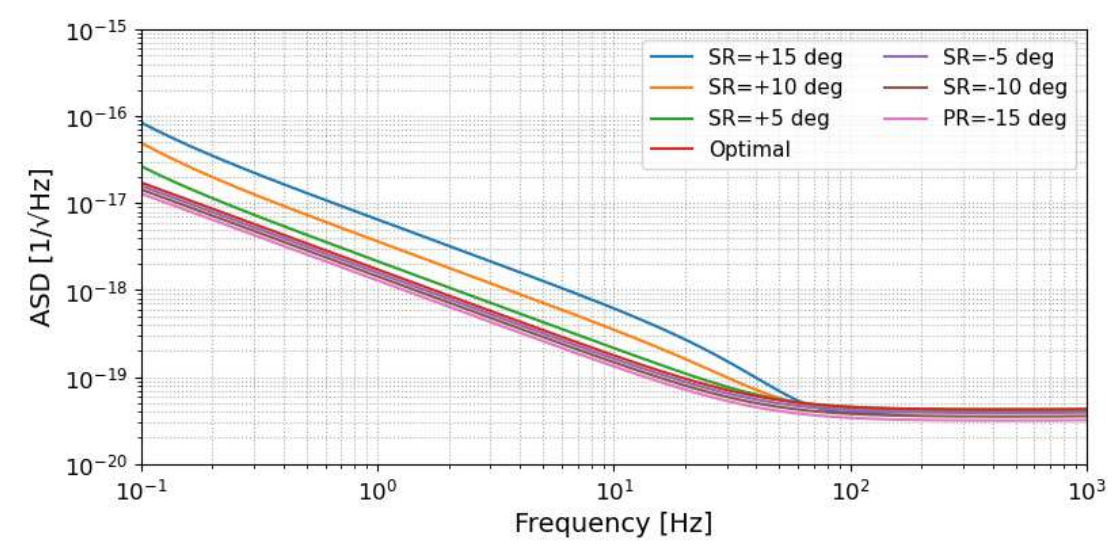


Figure 9: Impact of SRC detuning on shot noise. Detuning mixes amplitude and phase quadratures, introducing low-frequency contributions in addition to high-frequency degradation.

particular band, but instead produces a uniform change in the overall shot-noise level.

Figure 10 illustrates the corresponding impact on radiation-pressure noise. In a Sagnac speed-meter interferometer, radiation-pressure noise exhibits a characteristic transition from  $1/f^2$  to 1/f scaling at low frequencies. At resonance, the transition frequency is optimized so that radiation-pressure noise is minimized around 1 Hz. However, detuning the SRC alters the balance between the amplitude and phase quadratures, breaking the quantum non-demolition (QND) correlation that cancels back-action. Consequently, radiation-pressure noise increases at low frequencies, degrading the sub-hertz sensitivity that is critical for CHRONOS.

Figure 11 presents the total noise spectrum, including shot noise, radiation-pressure noise, and technical noise sources such as seismic and suspension noise. At  $\phi_s = 0$ , these contributions are balanced, yielding the best sensitivity in the 1–10 Hz band. When the SRC is detuned, however, the QND correlation is lost, and a marked degradation occurs in this frequency range. Therefore, CHRONOS adopts operation at the resonant condition ( $\phi_s = 90^{\circ}$  in our convention), which avoids the 1–10 Hz degradation and maximizes sub-hertz sensitivity.

It is worth noting that in longer-baseline interferometers, such as the 300 m-scale system studied by Inoue et al. [7], a small optimal detuning of approximately 2° has been identified. In that regime, the suppression of coating-induced time-delay effects becomes sufficient, and a small SRC detuning can slightly enhance the sensitivity. However, for the 2.5 m CHRONOS prototype, maintaining the exact resonance condition is most effective for preserving QND back-action cancellation and achieving quantum-noise-limited operation.

#### E. Impact of Homodyne Detection Angle

In this analysis, the homodyne detection angle  $\zeta$  is varied **around the** 90° **reference point**, which corresponds to the phase quadrature in the CHRONOS convention. This definition ensures consistency with the detuning-phase conventions used for the power- and signal-recycling cavities. All spectra in Figs. 12–14 are therefore plotted with respect to this 90° baseline.

The homodyne detection angle  $\zeta$  determines the quadrature of the output field that is measured in the balanced homodyne detector (BHD). By adjusting  $\zeta$ , the interferometer effectively changes the relative weighting between the amplitude  $(a_1)$  and phase  $(a_2)$  quadratures in the readout. This tuning allows the measured signal to emphasize either the shot-noise or radiation-pressure-noise contribution, depending on the chosen detection quadrature [29, 37].

Figure 12 shows the dependence of shot noise on the homodyne angle. Near the phase quadrature ( $\zeta \approx 90^{\circ}$ ), the shot noise dominates at high frequencies, and the amplitude spectral density remains nearly flat across the detection band. As the angle is rotated around the 90° phase point—defined as the reference quadrature in CHRONOS—the readout mixes the amplitude component ( $a_1$ ) into the detected signal. This corresponds to a quadrature rotation about 90° in phase space, which uniformly changes the overall level of shot noise across the entire frequency band without introducing strong frequency dependence. Thus, the variation of  $\zeta$  around 90° primarily acts as a global scaling of the shot-noise contribution rather than altering its spectral shape.

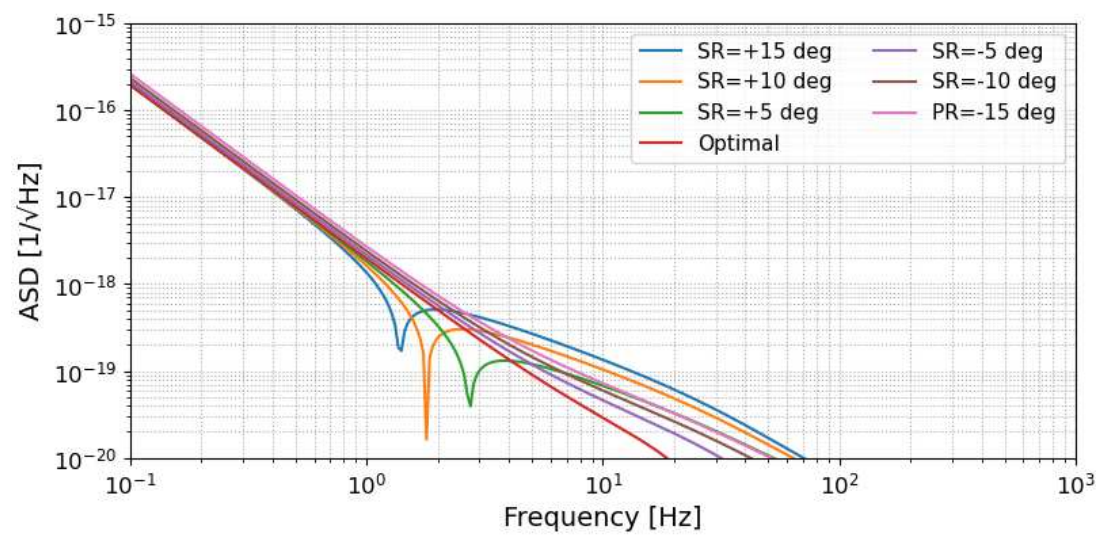


Figure 10: Impact of SRC detuning on radiation-pressure noise. The turnover frequency from  $1/f^2$  to 1/f scaling shifts depending on the detuning angle.

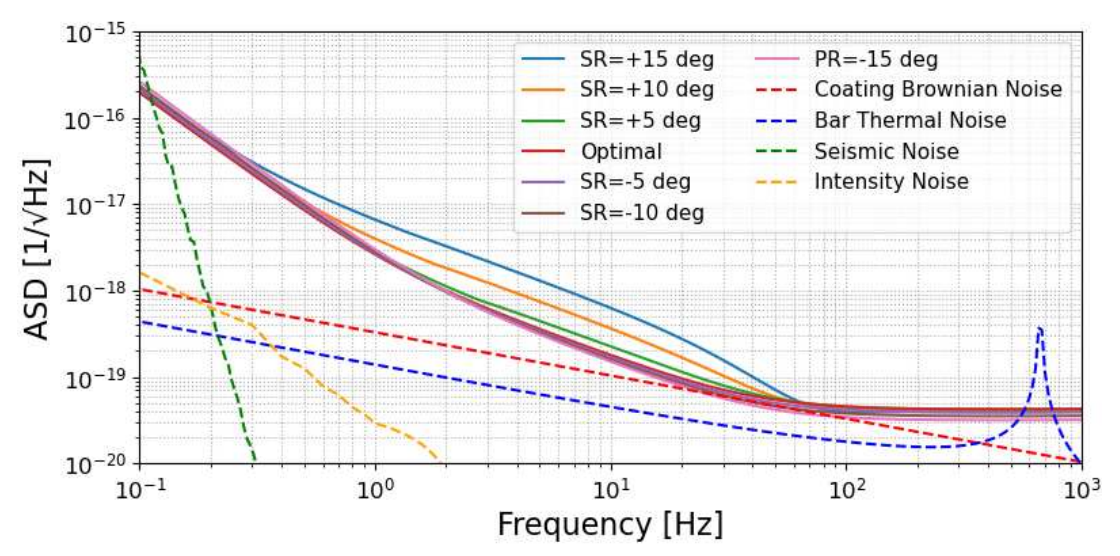


Figure 11: Total quantum-noise spectrum including shot noise, radiation-pressure noise, and technical noise. At resonance, the three contributions balance near 1–10 Hz, while detuning leads to significant degradation. The intensity noise is calculated in elsewhere [34]

Figure 13 illustrates the corresponding radiation-pressure noise. At  $\zeta=90^\circ$ , the interferometer operates as an ideal speed meter, coherently cancelling radiation-pressure noise in the mid-frequency band. At lower frequencies, however, the QND condition is partially broken due to coating-induced time-delay effects in the end test masses (ETMs), and the residual  $1/f^2$  component becomes visible. The transition frequency between the QND (back-action evasion) regime and the  $1/f^2$  region depends sensitively on the homodyne angle  $\zeta$ . By fine-tuning  $\zeta$ , the interferometer can extend the frequency range over which the QND cancellation remains effective, thereby broadening the low-noise region of CHRONOS.

The combined quantum-noise spectra are shown in Fig. 14. The optimal homodyne angle is found to be  $\zeta_{\rm opt} \simeq 46^{\circ}$ , where the trade-off between radiation-pressure suppression and shot-noise minimization yields the best overall sensitivity around 1 Hz. This configuration also ensures robust operation against optical gain fluctuations. Angles significantly smaller than 40° or larger than 60° result in degraded performance, demonstrating that precise control of the homodyne phase is essential for maintaining quantum-noise-limited operation in CHRONOS.

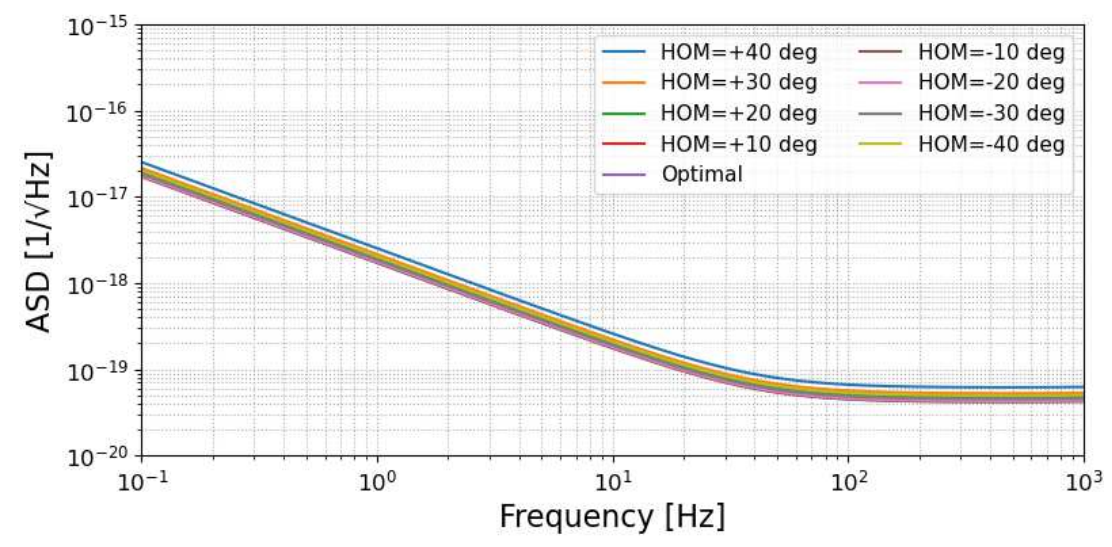


Figure 12: Dependence of shot noise on the homodyne detection angle  $\zeta$ . At smaller angles, amplitude-phase mixing produces interference minima but worsens the overall sensitivity at high frequencies.

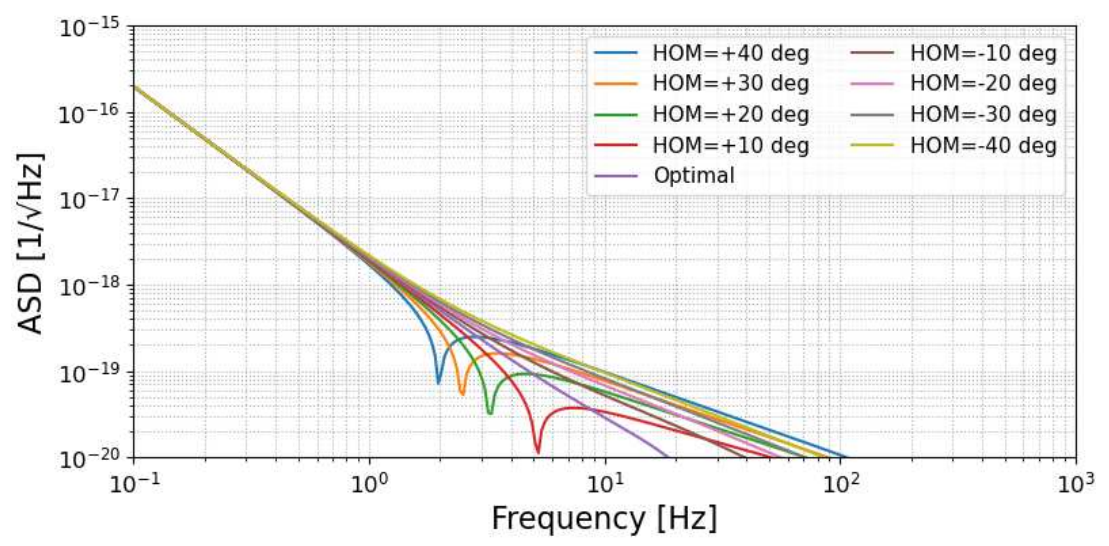


Figure 13: Radiation-pressure noise as a function of homodyne angle. The low-frequency suppression observed near  $\zeta = 90^{\circ}$  gradually weakens as the detection angle shifts toward the amplitude quadrature.

## VII. DISCUSSION

The sensitivity study presented here is optimized for the low-frequency band, reflecting the primary motivation of CHRONOS to probe the sub-hertz regime. In this configuration, the interferometer improves radiation-pressure-noise performance and demonstrates the feasibility of quantum-noise-limited operation at the 2.5 m scale. At the same time, it is important to emphasize that an alternative design optimized for higher frequencies could open a different range of scientific opportunities. By adjusting the detuning of the recycling cavities and the homodyne detection angle, the quantum-noise spectrum can be reshaped into a shot-noise-dominated form, enabling studies of short-duration or high-frequency signals.

Realizing such flexibility requires auxiliary optical systems in addition to the main interferometer. In particular, a dedicated alignment system using a green laser and wavefront sensors (WFS) is necessary. Given the relatively low transmissivity of the PRC input mirror, such systems are essential for maintaining mode matching and cavity stability. These subsystems are also crucial for ensuring robust operation and reliable calibration in the presence of environmental disturbances.

It must also be noted that our discussion is restricted to the 2.5 m laboratory-scale facility. While this configuration

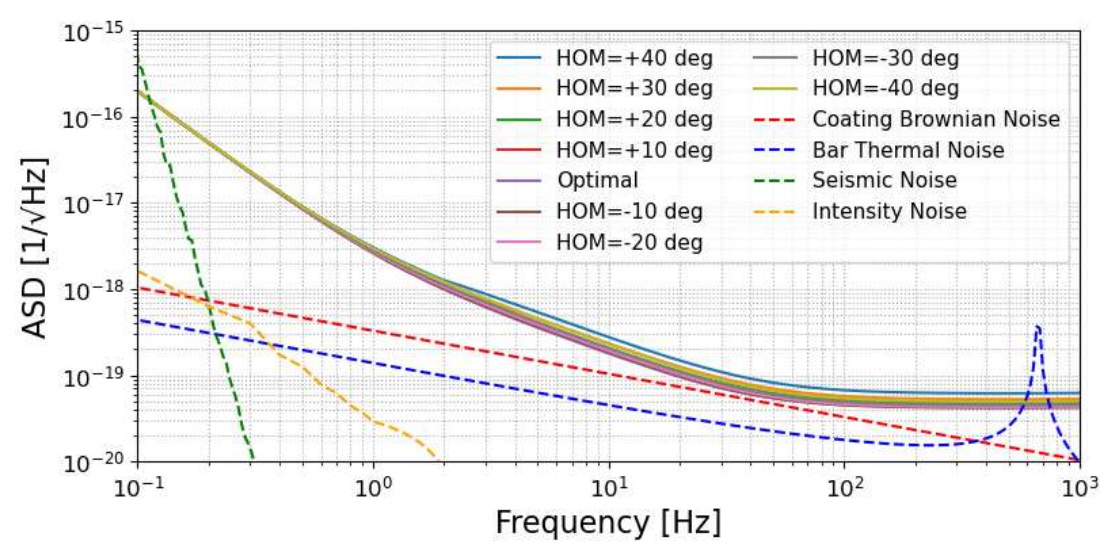


Figure 14: Total quantum-noise spectra for various homodyne angles. The optimal configuration at  $\zeta_{\rm opt} \simeq 46^{\circ}$  achieves balanced suppression of radiation-pressure and shot noise, yielding the best sensitivity near 1 Hz. The intensity noise is calculated in elsewhere [34].

allows detailed investigation of quantum-noise shaping and control techniques, scaling the arm length inevitably alters the balance of noise contributions. Among these, coating thermal noise remains a decisive factor. Even at the 2.5-m scale, the choice of coating technology—mechanical loss, thickness, and deposition method—directly determines the mid-band sensitivity floor [32, 33]. Future advances in low-loss coating materials will therefore be indispensable for realizing the scientific goals of CHRONOS and extending the design to larger-scale detectors.

At the laboratory scale, the first scientific opportunities are expected to arise from improved understanding of Newtonian noise and the potential detection of local seismic signals. The 2.5 m system provides a flexible platform in which optical and mechanical parameters can be tuned according to experimental goals. This adaptability enables CHRONOS to function not only as a testbed for precision quantum-noise studies but also as a practical tool for probing environmental signals, with parameter choices adjusted to specific situations.

In conclusion, the optical design and sensitivity modeling presented here establish the foundation of CHRONOS as a versatile sub-hertz interferometer. Although its scale is limited, the 2.5-m system highlights key trade-offs in cavity detuning, detection quadrature, and coating technology, providing valuable guidance for both laboratory-scale research and the path toward future long-baseline detectors.

## VIII. CONCLUSION

In this work, we have presented the optical design and sensitivity modeling of the 2.5 m CHRONOS interferometer, a laboratory-scale triangular Sagnac speed-meter interferometer incorporating both power- and signal-recycling techniques. Using a combination of ABCD-matrix analysis and FINESSE3 simulations, we demonstrated that stable eigenmodes can be realized with optimized radii of curvature and focal placement, leading to mode-matching efficiencies exceeding 99.5% across all major junctions.

The optimized configuration predicts a quantum-noise-limited strain sensitivity of

$$h \simeq 3 \times 10^{-18} \text{ Hz}^{-1/2}$$
 at 1 Hz, (25)

with a ring-cavity finesse of  $\mathcal{F} \simeq 3.1 \times 10^4$  and a round-trip Gouy phase of  $\psi_{\rm rt} \approx 153^\circ$ . The power-recycling cavity (PRC) detuning, optimized at  $\phi_p = -85^\circ$ , was identified as the dominant factor shaping the low-frequency quantum noise, while the signal-recycling cavity (SRC) detuning ( $\phi_s = 0^\circ$ ) introduces a uniform quadrature rotation around 90° without improving sensitivity. The optimal homodyne detection angle was determined to be  $\zeta_{\rm opt} \simeq 46^\circ$ , where the trade-off between radiation-pressure suppression and shot-noise minimization yields the best overall sensitivity near 1 Hz.

For the end test masses (ETMs), a target reflectivity of  $R_{\rm ETM} = 99.9999\%$  is assumed. However, optical absorption in the coatings remains the dominant limitation to the overall sensitivity, particularly under cryogenic operation

around 10 K. Further development of low-absorption dielectric materials such as SiN and SiON will therefore be indispensable for extending CHRONOS toward next-generation cryogenic detectors.

The analysis also indicates that low-frequency optimization effectively mitigates radiation-pressure noise in the sub-hertz band, while alternative parameter configurations—through controlled changes in detuning and homodyne phase—could enhance sensitivity at higher frequencies. Auxiliary optical systems, including green-laser alignment and wavefront sensing, are crucial for maintaining mode matching and stable operation in this regime.

The 2.5 m CHRONOS interferometer thus serves as both a versatile testbed for precision quantum-noise studies and a practical platform for environmental-noise investigations. The system exhibits high optical stability ( $\psi_{\rm rt} \approx 153^{\circ}$ ), large finesse ( $\mathcal{F} \approx 3 \times 10^{4}$ ), and sub-hertz quantum-limited sensitivity of  $3 \times 10^{-18}$  Hz<sup>-1/2</sup> at 1 Hz. These results establish a solid foundation for scaling CHRONOS toward longer-baseline facilities, bridging laboratory-scale quantum optics with the development of next-generation sub-hertz gravitational-wave observatories.

## ACKNOWLEDGMENTS

We also thank Kin-Wang Ng and Masashi Hazumi for their academic advice during the preparation of this manuscript. We thank Masaya Hasegawa, Takahiro Kanayama, Satoki Matsushita, Hirokazu Murakami, Mai Inoue, Ryuji Shibuya and Chia-Ming Kuo for support to establish CHRONOS team. Y.I. and H.W. acknowledges support from NSTC, CHiP and Academia Sinica in Taiwan under Grant No.114-2112-M-008-006-, and No.AS-TP-112-M01.

## Appendix A: Complete Optical Element Parameters

Table VI lists the full set of optical elements used in the 2.5 m CHRONOS interferometer, including their coordinates, incidence angles, curvature radii, and reflectivities. For brevity, power transmissivity and absorption values are omitted; they can be obtained from the relation T = 1 - R - A, with  $A \approx 0$ .

#### Appendix B: Noise Model

This appendix summarizes the principal technical noise models included in the sensitivity analysis. All contributions are normalized to the detector output using the frequency-dependent sensitivity transfer function  $H_{\text{sens}}(f)$  and the arm length  $L_{\text{arm}}$ .

# 1. Coating Brownian noise

Brownian motion arising from the dielectric coating of the ETMs is one of the dominant fundamental noise sources in the mid-frequency band of CHRONOS. This arises from microscopic mechanical dissipation in the high-reflectivity multilayer coating, which drives thermally induced surface displacement through the fluctuation-dissipation theorem [32, 33]. In the CHRONOS design, the interferometer response is ultimately limited by this process at frequencies where seismic and suspension noise are already suppressed and radiation-pressure noise is no longer dominant.

We evaluate the coating Brownian noise using the equivalent spring model in the half-infinite substrate approximation. The one-sided amplitude spectral density of the displacement noise, referred to the differential arm readout, is written as

$$S_{\text{coat}}(f) = \frac{1}{L_{\text{arm}}} \sqrt{\frac{2k_{\text{B}}T}{\pi^2 f}} \sqrt{\frac{1 - \sigma_s^2}{\omega_{\text{ETM}} Y_s}} \sqrt{\phi_c^{\text{eff}}}.$$
 (B1)

Here:

- $L_{\rm arm}$  is the effective arm length of the torsion bar. The prefactor  $1/L_{\rm arm}$  converts the strain noise of the ETM surface into an equivalent strain noise.
- $k_{\rm B}$  is Boltzmann's constant, and T is the temperature of the coating (cryogenic in the CHRONOS configuration). The scaling  $\propto \sqrt{T}$  explicitly shows why cryogenic operation is essential for suppressing coating Brownian noise.
- $\sigma_s$  and  $Y_s$  are the Poisson ratio and Young's modulus of the ETM substrate, respectively. These elastic parameters determine how efficiently internal mechanical loss in the coating is converted into surface motion.

Table VI: Full list of optical elements in the CHRONOS 2.5 m. The corresponding optical components are shown in Fig. 2. Incident angle in degrees, curvature radius in meters, and power reflectivity R. Based on the length of Ring cavity, PRC, and SRC, the optimized radius of curvature is listed.

Name	Incident angle [°]	Radius of curvature [m]	Reflectivity R
ETMLY	1.21	2.69	0.999999
ETMRY	1.21	2.69	0.999999
MTMLY	37.33	$\infty$	0.999999
MTMRY	37.33	$\infty$	0.999999
ITMLY	51.46	$\infty$	0.9999
ITMRY	51.46	$\infty$	0.9999
CMRY	7.57	0.141	0.999999
CMLY	7.57	0.141	0.999999
BSY	0.00	$\infty$	0.5
BSMLY	23.14	$\infty$	0.999999
BSMRY	23.14	$\infty$	0.999999
SRMY3	26.27	$\infty$	0.999999
SRMY2	26.02	7.15	0.999999
SRMY1	0.00	$\infty$	0.5
PRMY4	26.02	∞ 7.00	0.999999
PRMY3	3.77	7.02	0.999999
PRMY2	45.00	$\infty$	0.999999
PRMY1 OMY	0.00 45.00	∞	0.9 $0.999999$
ETMLX	1.21	$ \begin{array}{c} \infty \\ 2.69 \end{array} $	0.999999
ETMRX	1.21	2.69	0.999999
MTMLX	37.33	∞	0.999999
MTMRX	37.33	$\infty$	0.999999
ITMLX	51.46	∞	0.9999
ITMRX	51.46	$\infty$	0.9999
CMRX	7.57	0.141	0.999999
CMLX	7.57	0.141	0.999999
BSX	0.00	$\infty$	0.5
BSMLX	23.14	$\infty$	0.999999
BSMRX	23.14	$\infty$	0.999999
SRMX3	26.27	$\infty$	0.999999
SRMX2	3.77	7.15	0.999999
SRMX1	0.00	$\infty$	0.5
PRMX4	26.27	$\infty$	0.999999
PRMX3	3.77	7.02	0.999999
PRMX2	45.00	$\infty$	0.999999
PRMX1	0.00	$\infty$	0.9
OMX	45.00	$\infty$	0.999999
IBS	45.00	$\infty$	0.999999
IMM2	7.85	$\infty$	0.999999
IMM1	7.85	$\infty$	0.999999
OBS	45.00	$\infty$	0.999999
IMC1	2.25	$\infty$	0.999999
IMC2	2.25	∞ 40.00	0.999999
IMC3	2.25	40.00	0.999999
IMC4	2.25	40.00	0.999999

- $\omega_{\text{ETM}}$  is a geometric factor set by the spatial profile of the sensing beam on the mirror surface. For a Gaussian interrogation beam,  $\omega_{\text{ETM}}$  is approximately proportional to the beam radius w on the ETM. A larger beam radius averages over a wider area and thereby reduces the coupling to local coating fluctuations.
- $\phi_c^{\text{eff}}$  is the effective mechanical loss angle of the coating stack. This term incorporates the individual loss angles, thicknesses, and elastic moduli of the high-index and low-index layers in the dielectric mirror coating. Multilayer designs with low-loss (e.g., SiN/SiON) materials reduce  $\phi_c^{\text{eff}}$  and thus directly improve sensitivity.

The  $f^{-1/2}$  scaling of  $S_{\rm coat}(f)$  reflects the thermally driven random force spectrum acting on a mechanically lossy elastic system. In CHRONOS, this contribution sets the practical noise floor in the mid-frequency range (roughly  $\sim 1$ –10 Hz), where radiation-pressure noise has begun to decouple due to the speed-meter topology, but seismic and suspension noise are already strongly attenuated. Consequently, coating Brownian noise defines one of the key material-driven limits to the interferometer performance and directly motivates the use of cryogenic, low-loss coating technologies (Sec. A and Sec. VI A).

## 2. Bar Thermal Noise (Torsion Bar)

The torsion-bar thermal noise model combines two principal contributions: (1) the broadband structural damping arising from internal material loss of the suspension and bar body, and (2) the narrow-band angular thermal noise peaking near the torsional resonance frequency [42, 44]. These two effects together describe both the wideband background and the resonant thermal motion of the torsion bar.

The total one-sided amplitude spectral density of the equivalent displacement noise is expressed as

$$S_{\text{bar,bg}}(f) = \sqrt{\frac{2k_{\text{B}}T}{\pi^{3/2}f}} \sqrt{\frac{1 - \sigma_s^2}{\omega_{\text{ETM}} Y_s}} \sqrt{\phi_s^{\text{eff}}},$$
(B2)

$$S_{\text{bar,rot}}(f) = \sqrt{\frac{4k_{\text{B}}T}{I}} \sqrt{\frac{\eta^2 \omega_{\text{tb}} \phi_0}{(\omega_{\text{tb}}^2 - \omega^2)^2 + \omega \omega_{\text{tb}} \phi_0}},$$
(B3)

$$S_{\text{bar}}(f) = \frac{1}{L_{\text{arm}}} \sqrt{S_{\text{bar,bg}}^2 + S_{\text{bar,rot}}^2}.$$
 (B4)

Here  $\omega = 2\pi f$ ,  $\omega_{\rm tb}$  is the torsional resonance angular frequency,  $\phi_s^{\rm eff}$  is the effective material loss angle,  $\phi_0$  represents the loss parameter associated with the resonance peak,  $\eta$  denotes the coupling efficiency between the bar rotation and interferometer readout, and I is the moment of inertia of the torsion bar.

The first term,  $S_{\rm bar,bg}$ , represents the broadband contribution arising from structural damping and internal friction of the suspension fibers or bar material. It exhibits a characteristic  $f^{-1/2}$  dependence typical of thermally driven losses. The second term,  $S_{\rm bar,rot}$ , describes the resonant enhancement near  $\omega \approx \omega_{\rm tb}$ , reflecting the thermal excitation of the torsional eigenmode. At frequencies well below resonance,  $S_{\rm bar,rot}$  scales approximately as  $f^{-1}$ , while above resonance it decreases as  $f^{-3}$ , consistent with the mechanical response of a torsional oscillator.

The total contribution  $S_{\rm bar}$  is converted to strain noise by dividing by the torsion bar arm length  $L_{\rm arm}$ . In CHRONOS, this term dominates below  $\sim 0.5$  Hz, where seismic noise and radiation-pressure noise are both suppressed. Minimizing the effective loss angles  $\phi_s^{\rm eff}$  and  $\phi_0$ , and maximizing the mechanical quality factor  $Q = 1/\phi_0$ , are therefore essential design goals for achieving the sub-hertz sensitivity required for CHRONOS.

## 3. Seismic Noise

Noise due to ground displacement couples into the detector output through the pre-isolation system and the suspension transfer functions [45, 46]. This coupling is especially critical in the sub-hertz band, where seismic motion dominates all other technical noise sources. In this study, the ground displacement spectrum measured at the AS-GRAF [47] site is adopted as the baseline input, combined with the modeled attenuation provided by the pre-isolation stage and the suspension system.

At low frequencies (f < 1 Hz), the system is assumed to employ a pre-isolation configuration analogous to that of LIGO, incorporating both passive and active isolation stages, followed by a multi-stage pendulum suspension. The overall transfer function thus includes the full yaw response of the suspension. For the rotational degree of freedom, the effective seismic coupling is empirically found to be roughly 1/100 of the translational coupling amplitude, consistent with the TOBA analysis [5].

The resulting one-sided amplitude spectral density of the seismic contribution is expressed as

$$S_{\text{seis}}(f) = \frac{1}{\omega} \frac{|H_{\text{yaw}}(f)|}{G_{ua}G_{\text{pre}}} S_x^{\text{ground}}(f), \tag{B5}$$

where:

- $S_x^{\text{ground}}(f)$  is the measured ground-displacement spectrum at the ASGRAF site, typically characterized by  $10^{-7}$ – $10^{-9}$  m/ $\sqrt{\text{Hz}}$  in the 0.1–10 Hz range.
- $H_{\text{yaw}}(f)$  is the suspension yaw transfer function, describing the angular response of the suspended bar to ground motion.
- $G_{\mu g}$  is the conversion gain between mechanical torque and equivalent gravitational acceleration, incorporating the bar geometry and lever arm.

•  $G_{\text{pre}}$  represents the frequency-dependent attenuation of the pre-isolation system, typically providing suppression proportional to  $f^{-4}$  to  $f^{-6}$  above the microseismic peak.

For the full CHRONOS facility, a dedicated vibration-isolation platform and cryogenic suspension are planned to achieve enhanced attenuation in the sub-hertz region. Such systems will combine multiple layers of active inertial sensing, low-frequency tilt decoupling, and cryogenic damping control to suppress seismic noise below  $10^{-18}$  m/ $\sqrt{\rm Hz}$  at frequencies approaching 0.1 Hz. These developments are essential for extending the CHRONOS sensitivity into the deep sub-hertz band, where Newtonian noise and coating thermal noise become the dominant limiting factors.

```
[1] B. P. Abbott et al., Phys. Rev. Lett. 116, 061102 (2016).
 [2] R. Abbott et al., Phys. Rev. X 11, 021053 (2021).
 [3] T. Akutsu et al., Nat. Astron. 3, 35 (2019).
 [4] P. Amaro-Seoane et al., (2017), arXiv:1702.00786.
 [5] M. Ando et al., Phys. Rev. Lett. 105, 161101 (2010).
 [6] D. J. McManus, et al., Phys. Rev. Lett. 118, 231101 (2017).
 [7] Y. Inoue et al., arXiv preprint arXiv:2509.23172 (2025), 10.48550/arXiv.2509.23172.
 [8] P. Amaro-Seoane et al., (2017), arXiv:1702.00786.
 [9] R. Abbott et al., (2021), arXiv:2111.03634.
[10] C. Caprini et al., J. Cosmol. Astropart. Phys. 2016, 001 (2016).
[11] K. K. Y. Ng et al., Phys. Rev. D 104, 083505 (2021).
[12] P. R. Saulson, Fundamentals of Interferometric Gravitational Wave Detectors (World Scientific, 1994).
[13] R. L. Forward, Phys. Rev. D 17, 379 (1978).
[14] J. Aasi et al., Class. Quantum Grav. 32, 074001 (2015).
[15] R. Abbott et al., Class. Quantum Grav. 38, 135014 (2021).
[16] Y. Chen, Phys. Rev. D 67, 122004 (2003).
[17] S. L. Danilishin and F. Y. Khalili, Living Rev. Relativ. 15, 5 (2012).
[18] J. Mizuno et al., Phys. Lett. A 175, 273 (1993).
[19] H. J. Kimble, Y. Levin, A. B. Matsko, K. S. Thorne, and S. P. Vyatchanin, Phys. Rev. D 65, 022002 (2001).
[20] T. Fricke et al., Class. Quantum Grav. 29, 065005 (2012).
[21] H. Vahlbruch, M. Mehmet, K. Danzmann, and R. Schnabel, Phys. Rev. Lett. 105, 131102 (2010).
[22] A. Buonanno and Y. Chen, Phys. Rev. D 67, 062002 (2003).
[23] P. Kwee, B. Willke, and K. Danzmann, Opt. Express 20, 10617 (2012).
[24] M. Evans, R. Sturani, N. Christensen, and et al., Phys. Rev. D 91, 022003 (2015).
[25] T. Akutsu, M. Ando, K. Arai, and et al., Prog. Theor. Exp. Phys. 2021, 05A101 (2021).
[26] R. W. P. Drever et al., Appl. Phys. B 31, 97 (1983).
[27] E. D. Black, Am. J. Phys. 69, 79 (2001).
[28] S. M. Aston et al., Class. Quantum Grav. 29, 235004 (2012).
[29] S. L. Danilishin, F. Y. Khalili, and H. Miao, Living Rev. Relativ. 22, 2 (2019).
[30] H. Kogelnik and T. Li, Appl. Opt. 5, 1550 (1966).
[31] F. Bayer-Helms, Appl. Opt. 23, 1369 (1984).
[32] G. M. Harry et al., Classical and Quantum Gravity 19, 897 (2002).
[33] Y. Levin, Phys. Rev. D 57, 659 (1998).
[34] D. Tanabe et al., "Title of the unpublished work (in preparation)," (2025), in preparation.
[35] C. M. Caves and B. L. Schumaker, Phys. Rev. A 23, 1693 (1981).
[36] V. B. Braginsky and F. Y. Khalili, Quantum Measurement (Cambridge University Press, Cambridge, 1992).
[37] A. Buonanno and Y. Chen, Physical Review D 64, 042006 (2001).
[38] P. Hello and J.-Y. Vinet, J. Phys. France 51, 2243 (1990).
[39] H. Pan et al., Physical Review D 97 (2018), 10.1103/PhysRevD.97.022004.
[40] S. Chao et al., Physical Review Letters 130 (2023), 10.1103/PhysRevLett.130.081403.
[41] V. Kumar et al., "Title of the unpublished work (in preparation)," (2025), in preparation.
[42] K. Yamamoto et al., Phys. Rev. D 74, 022002 (2006).
[43] I. W. Martin et al., Class. Quantum Grav. 27, 225020 (2010).
[44] P. R. Saulson, Phys. Rev. D 42, 2437 (1990).
[45] P. R. Saulson, Phys. Rev. D 30, 732 (1984).
[46] J. Harms, Living Rev. Relativ. 22, 6 (2019).
[47] "Academia Sinica GRAvitational research Facility (ASGRAF)," https://www.phys.sinica.edu.tw/~gravitation-physics/research
    accessed: 2025-09-26.
```